Direct and Rectified Effects of Tropical Instability Waves on the Eastern Tropical Pacific Mean State in a Regional Ocean Model

Lisa Maillard, Julien Boucharel, Lionel Renault

Direct and Rectified Effects of Tropical Instability Waves on the Eastern Tropical Pacific Mean State in a Regional Ocean Model

LISA MAILLARD,[a] JULIEN BOUCHAREL,[a,b] AND LIONEL RENAULT[a,c]

[a] *LEGOS, University of Toulouse, IRD, CNRS, CNES, UPS, Toulouse, France*
[b] *Department of Atmospheric Sciences, School of Ocean and Earth Science and Technology, University of Hawai'i at Mānoa, Honolulu, Hawaii*
[c] *Department of Atmospheric and Oceanic Sciences, University of California, Los Angeles, Los Angeles, California*

(Manuscript received 7 December 2021, in final form 27 April 2022)

ABSTRACT: Tropical instability waves (TIWs) are oceanic features propagating westward along the northern front of the Pacific cold tongue. Observational and modeling studies suggest that TIWs may have a large impact on the eastern tropical Pacific background state from seasonal to interannual time scales through heat advection and mixing. However, observations are coarse or limited to surface data, and modeling studies are often based on the comparison of low- versus high-resolution simulations. In this study, we perform a set of regional high-resolution ocean simulations (CROCO 1/12°) in which we strongly damp (NOTIWs-RUN) or not (TIWs-RUN) TIW propagation, by nudging meridional current velocities in the TIW region toward their monthly climatological values. This approach, while effectively removing TIW mesoscale activity, does not alter the model internal physics in particular related to the equatorial Kelvin wave dynamics. The impact of TIWs on the oceanic mean state is then assessed by comparing the two simulations. While the well-known direct effect of TIW heat advection is to weaken the meridional temperature gradient by warming up the cold tongue (0.34°C month^{-1}), the rectified effect of TIWs onto the mean state attenuates this direct effect by cooling down the cold tongue (−0.10°C month^{-1}). This rectified effect occurs through the TIW-induced deepening and weakening of the Equatorial Undercurrent, which subsequently modulates the mean zonal advection and counterbalances the TIWs' direct effect. This approach allows quantifying the rectified effect of TIWs without degrading the model horizontal resolution and may lead to a better characterization of the eastern tropical Pacific mean state and to the development of TIW parameterizations in Earth system models.

SIGNIFICANCE STATEMENT: Tropical instability waves (TIWs), meandering features at the surface of the equatorial Pacific Ocean, have long been recognized as a key component of the climate system that can even impact marine ecosystems. Yet, they are still hardly simulated in coupled global climate models. Here, we introduce a new framework to isolate and quantify their complex influence on the tropical Pacific background climate. This approach allows revealing a so far overlooked effect of TIWs on the mean circulation and heat transport in this region that should be accounted for in the next generation of global coupled climate models through parameterization or increased resolution.

KEYWORDS: Mesoscale processes; Ocean models; Tropical variability; Ocean dynamics; Heat budgets/fluxes

1. Introduction

Tropical instability waves (TIWs) are prominent oceanic mesoscale features that have been first observed in the 1970s in the eastern equatorial Pacific (Legeckis 1977) and Atlantic (Düing et al. 1975) Oceans. Since these seminal studies based on satellite and in situ measurements of sea surface temperature (SST) and currents, many efforts have been made to characterize the TIW cusp-shaped and meandering features through satellite and in situ observations of many other oceanic and atmospheric variables such as sea surface height (Miller et al. 1985; Malardé et al. 1987; Musman 1989; Périgaud 1990; Escobar-Franco et al. 2022), velocity (Halpern et al. 1988; Bryden and Brady 1989; Qiao and Weisberg 1995; McPhaden 1996; Kennan and Flament 2000), low-level wind and wind stress (Xie et al. 1998; Chelton et al. 2001; Hashizume et al. 2001), subsurface temperature (McPhaden 1996; Flament et al. 1996; Kennan and Flament 2000), and ocean color and related biogeochemical properties as well (Yoder et al. 1994; Chavez et al. 1999; Strutton et al. 2001; Legeckis et al. 2004; Evans et al. 2009). All these observational studies have contributed to a better understanding of the main properties of TIWs, which essentially represent the dominant form of eddy variability in the equatorial regions. In particular, TIWs are westward-propagating oscillations along the sharp temperature front between the cold upwelled equatorial waters and the warmer waters to the north. They usually appear in the eastern equatorial Pacific in June and persist until the beginning of the following year. Their wavelength is 800–2000 km, and their period is on the order of 15–40 days (Qiao and Weisberg 1995; Lyman et al. 2007). TIWs have very sharp fronts on the order of 100 km at their leading and trailing edges (Warner et al. 2018), associated with strong changes in temperature within a few kilometers.

Complementing these observational studies, early numerical studies (Philander 1976, 1978) started to investigate TIW

Denotes content that is immediately available upon publication as open access.

Corresponding author: Lisa Maillard, lisa.maillard@univ-tlse3.fr

DOI: 10.1175/JPO-D-21-0300.1

generating mechanisms. These forerunner modeling studies first revealed that TIWs arise from barotropic instability (i.e., a conversion from the mean kinetic energy to the eddy kinetic energy, EKE) due to the strong shears between the Equatorial Undercurrent (EUC) and South Equatorial Current (SEC), as well as between the SEC and North Equatorial Countercurrent (NECC), yet to a lesser extent. Later, other idealized modeling and linear stability analyses (Cox 1980; Yu et al. 1995) suggested that baroclinic, Kelvin–Helmholtz, and frontal instabilities also greatly contributed to the generation of TIWs. The induced conversion from available eddy potential energy to EKE was shown to be caused by the sharp meridional gradient of SST between the cold tongue and the surrounding warmer waters (Masina et al. 1999; Im et al. 2012). TIWs have been shown to strongly interact with the atmosphere by exchanging momentum and heat fluxes. Seo et al. (2007) show that TIWs affect the turbulent heat fluxes while Small et al. (2009) demonstrate that TIWs, through the influence of the surface current on the atmosphere (current feedback, e.g., Renault et al. 2016), are damped by 10% or more.

TIW activity is strongly modulated by changes in the climate background over a wide range of time scales. At seasonal time scales, the trade winds intensification during the second half of the year increases the Ekman divergence of surface water. This promotes a colder cold tongue through intensified equatorial upwelling and therefore a stronger meridional SST gradient. In addition, the intensified trade winds also strengthen the SEC. This triggers an increase in both frontal and current shear instabilities, resulting in more kinetic energy production and thus enhanced TIW activity from July to February of the following year (Contreras 2002; von Schuckmann et al. 2008; Wang et al. 2017, 2019). At interannual time scale, TIW activity in the Pacific Ocean is mostly modulated by El Niño–Southern Oscillation (ENSO). In particular, La Niña conditions are accompanied by an increase in meridional SST gradient and intensified currents near the eastern tropical Pacific, which strengthen TIW variability (Hashizume et al. 2001; Yu and Liu 2003). On the other hand, during the warm El Niño phase, the thermocline deepens in the east and warmer waters are brought into the cold tongue, reducing the meridional temperature gradient and concurrently the TIW activity (Philander 1990; Vialard et al. 2001). At intraseasonal time scales, Harrison and Giese (1988) and Giese and Harrison (1991) uncovered changes in TIW amplitude as a response to the passage of Kelvin waves. More recently, the theoretical work by Holmes and Thomas (2016) further revealed that the presence of Kelvin waves could disrupt zonal currents background and in turn modulate the lateral shear production and related TIW generation, with in particular a decreased (strengthened) TIW activity during the downwelling (upwelling) intraseasonal Kelvin waves phase, which has been further confirmed by Escobar-Franco et al. (2022) in satellite observations.

TIWs have been shown to influence the climate state through eddy heat flux convergence and induced nonlinear dynamical heating (Holmes and Thomas 2015; Jin 2003). TIWs have a direct effect on the mean state through nonlinear eddy processes and a rectified effect through upscaling feedbacks, i.e., integrated effects of eddies over a long period of time. For instance, TIWs have been shown to warm up the equatorial cold tongue through the direct effect of horizontal advection of heat by anomalous currents at a rate of approximately 1°C month^{-1}, counterbalancing the cooling induced by mean currents and vertical mixing (Menkes et al. 2006; Im et al. 2012), and highlighting a seasonally modulated negative feedback in the eastern tropical Pacific. Similarly, the ENSO–
TIWs relationship described above has been shown to be modulated at interannual time scales, this feedback being stronger during La Niña than during El Niño, therefore promoting an anomalous mean state warming (cooling) during ENSO negative (positive) phase (An 2008; Imada and Kimoto 2012; Graham 2014). This suggests that TIWs act as an asymmetric negative feedback onto ENSO and influence the cold tongue interannual mean state through a nonlinear rectifying feedback (Boucharel and Jin 2020; Xue et al. 2020, 2021). To sum up, TIWs are at the heart of complex two-way cascading multiscale interactions playing out in the eastern tropical Pacific, which makes it extremely difficult to properly disentangle the direct from the rectified TIW effects onto this region's mean state.

Nonetheless, a few modeling studies have attempted to tackle this issue opting for two different avenues to characterize TIW effects onto the mean, seasonal and interannual cold tongue climate: 1) through the comparison of eddy-permitting or resolving (in which TIWs are free to develop) versus eddy-nonpermitting (i.e., with a resolution too coarse for TIWs to be generated) global ocean model (Graham 2014; Roberts et al. 2004, 2009) and 2) through the implementation of a simple TIW parameterization (mesoscale eddy parameterization of the isopycnal-layer thickness diffusion coefficient, originally developed for baroclinic fronts at mid- or high latitudes; Gent and McWilliams 1990; Gent et al. 1995; Bryan et al. 1999) into an eddy-nonpermitting atmosphere–ocean general circulation model (Imada and Kimoto 2012). The results of these studies suggest that the presence of TIWs (either parameterized or at least partly resolved in the higher spatial resolution model) acts to reduce the equatorial cold tongue well-known cold bias and improve ENSO asymmetry. Yet, one can wonder if these observed differences really originate from only TIW-induced effects or also from a combination of counterbalancing effects due to the altered dynamic triggered by drastic changes in spatial resolution or by the parameterization's intrusive effects?

In this study, motivated by these legitimate interrogations, we develop a new framework to accurately delineate the direct and rectified effects of TIWs onto the ocean mean dynamics. This method is based upon the removal of TIWs in the eastern tropical Pacific by nudging the meridional currents toward their monthly climatological values in an eddy-rich oceanic model. This approach contrasts with the usual technique involving comparison of low- versus high-resolution simulations evoked above, in the sense that small-scale processes and other potential bathymetry-induced instabilities are kept untouched here. This allows quantifying the direct and rectified effects

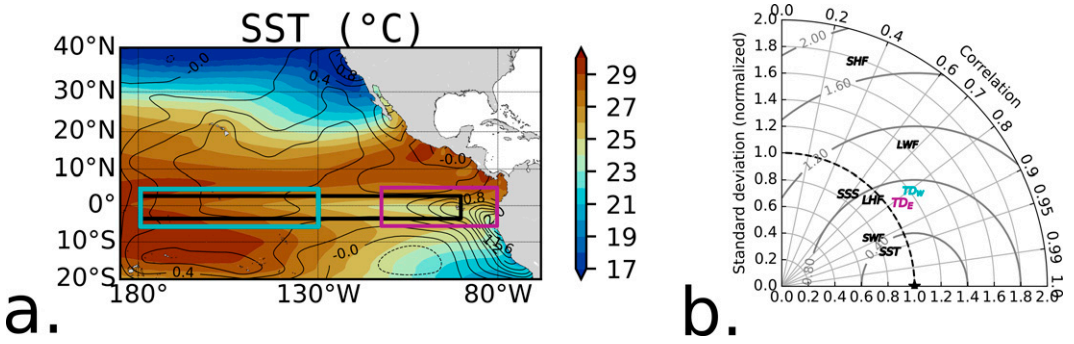

FIG. 1. Evaluation of simulated SST, SSS, and heat fluxes in the control experiment TIWs-RUN. (a) Shading shows the mean SST in the model. Solid and dashed contours (every 0.2°C) show, respectively, the positive and negative mean bias between the model and observed SST. (b) Taylor diagram of SST, SSS, latent heat flux (LHF), sensible heat flux (SHF), shortwave radiation (SWF), and longwave radiation (LWF) monthly time series averaged in the region [2°S–2°N, 180°–90°W, black box in (a)] and thermocline depth (calculated as the depth of the 20°C isotherm) averaged in eastern [TD_E: 3°S–3°N, 110°–80°W, purple box in (a)] and western [TD_W: 3°S–3°N, 180°–140°W, blue box in (a)] regions. Tracers are compared to SODA v3.4.2 during 1980–2019 and fluxes are compared to TropFlux during 1980–2018. Observations are indicated by the black star in the diagram. The angular coordinate shows the Pearson correlation coefficient between the model and observations. The radial coordinate shows the standard deviation normalized by the observations. Gray circles indicate the root-mean-square error between model and observations.

associated with TIW variability on the eastern Pacific mean state and circulation. The paper is structured as follows: section 2 describes the data and model. In section 3, an evaluation of the model performance is done by comparing simulated temperature, fluxes, currents, and mesoscale activity to available observational data. Section 4 describes and validates thoroughly our methodology. In section 5, TIW direct and rectified effects on the oceanic mean state and dynamics are assessed through a heat budget analysis. Results are summarized and discussed in section 6.

2. Model configuration and methods

a. Coastal and Regional Ocean Community model

The oceanic simulations were performed with the Coastal and Regional Ocean Community (CROCO) model (Shchepetkin and McWilliams 2005, 2009; Debreu et al. 2012; Shchepetkin 2015). CROCO is a free-surface, terrain-following coordinate model with split-explicit time stepping and with Boussinesq and hydrostatic approximations. CROCO is implemented over the eastern tropical Pacific from the central Pacific to the American continent (Fig. 1a) i.e., from 185° to 68°W and from 20°S to 40°N at a spatial resolution of 1/12°, corresponding roughly to 9.3 km at the equator. Tracers, surface elevation, and horizontal velocity initial and boundary information are derived from the Simple Ocean Data Assimilation 5-day reanalysis (SODA v3.4.2 on a 1/4° × 1/4° grid; Carton et al. 2019). Because the SODA and model grids rely on different coordinate systems (terrain following vs z coordinates), pressure gradient artifacts can appear, potentially creating spurious rim currents. To avoid this issue, the model grid is merged toward SODA's along the open boundaries (over approximately a 3° band in latitude and a 6° band in longitude). A sponge layer is also applied to enhance the viscosity and diffusivity near the boundary. The configuration has 50 vertical σ levels and the vertical grid is stretched for increased boundary layer resolution using stretching surface and bottom parameters of $h_{\text{cline}} = 200$ m, $\theta_b = 2$, and $\theta_s = 7$. The bathymetry is obtained from the Shuttle Radar Topography Mission (SRTM30 plus; Becker et al. 2009). To avoid aliasing and to ensure the smoothness of the topography at the grid scale, a Gaussian smoothing kernel with a width of 8 times the topographic grid spacing is used.

Vertical mixing of tracers and momentum is done with a K-profile parameterization (KPP; Large et al. 1994). The surface freshwater, heat, and momentum fluxes are estimated using the COARE bulk formulae (Fairall et al. 2003). The atmospheric surface fields are derived from the hourly Climate Forecast System Reanalysis (CFSR; Saha et al. 2010, 2011). We use in particular CFSR from 1980 to 2010 and CFSRv2 onward. The essential atmospheric fields for the ocean-only models are the precipitation rate, the wind field at 10 m, the shortwave and longwave radiation flux, and the temperature and specific humidity at 2 m. To have a realistic representation of the mesoscale activity and of the momentum exchange between the ocean and the atmosphere, the surface oceanic current feedback to the atmosphere (Renault et al. 2016) is parameterized using the stress-correction approach described in Renault et al. (2020).

Two simulations are carried out over the period 1980–2019 after a spinup of seven years, until the total kinetic energy stabilizes. The control simulation, where TIWs are free to develop and propagate, is called TIWs-RUN. The simulation in which TIWs are damped is called NOTIWs-RUN. Offline calculations are made using model outputs at daily average and 1/12° spatial resolution.

b. Observational data

We use a variety of in situ and satellite observational data to validate the model control simulation:

- SST data come from the NOAA 1° Optimal Interpolation of SST version 2 (OI SST v2) data product obtained from in situ and satellite measurements from 1981 to nowadays.
- The SST, sea surface salinity (SSS), and thermocline temporal variabilities are evaluated using SODA v3.4.2 reanalysis on a 1/4° × 1/4° grid, over the 1980–2019 period.
- Heat and momentum fluxes are obtained from TropFlux product on a 1° × 1° grid, from 1980 to 2018. This product combines ERA-Interim and International Satellite Cloud Climatology (ISCCP) data to derive air–sea fluxes (Praveen Kumar et al. 2012). We also used the COREv2 product on a 1° × 1° grid (Yeager and Large 2008).
- In-depth currents come from Johnson's climatology (Johnson et al. 2002), which is derived from in situ measurements of upper-ocean currents in the tropical Pacific during the 1990s.
- Surface currents are obtained from the NOAA 1/4° drifter database (Laurindo et al. 2017), in which the global near-surface currents are derived from satellite-tracked surface drifting buoy observations.
- The eddy kinetic energy is computed using daily mean surface currents from the Copernicus Marine Environment Monitoring Service (CMEMS) on a 1/4° × 1/4° grid (Rio et al. 2014).

c. Intraseasonal anomalies

To capture the variability associated with TIWs, which have periods ranging from 15 to 35 days (Lyman et al. 2007; Wang et al. 2020), anomalies are defined as fluctuations from a 30-day running mean.

d. Statistical significance

The significance of differences between the two simulations is evaluated by generating 40 samples of annual differences (i.e., one for each of the simulation's 40 years) on which a two-tailed Student's t test at 99% is performed, the null hypothesis being a difference of zero. The significance of curves is done using a bootstrapping of the annual means of the variable of interest, i.e., 40 samples, and repeated 1000 times.

e. Heat budget

To assess how TIWs impact the eastern Pacific mean state through changes in the dynamical processes balance, the following temperature heat budget is computed:

$$\underbrace{\frac{\partial T}{\partial t}}_{\text{Tendency}} = -\underbrace{(\mathbf{u}\nabla T)}_{\text{Advection}} + \underbrace{D_l(T)}_{\text{Lateral mixing}} + \underbrace{D_z(T)}_{\text{Vertical mixing}} + \underbrace{I(z)}_{\text{Atmospheric forcing}}, \tag{1}$$

where T is the ocean temperature; $\mathbf{u}$ is the current vector; ∇ is the spatial gradient; $D_l(T)$ and $D_z(T) = \partial_z(k\partial_z T)$ the lateral and vertical mixing terms, respectively; and $I(z)$ is the heating by atmospheric forcing (i.e., solar radiation and its penetration in depth).

We focus on the 50-m surface layer. The integration with depth is denoted $\langle x\rangle = (1/h)\int_0^h x\,dz$ with $h = 50$ m. It gives

$$\frac{\partial\langle T\rangle}{\partial t} = -\langle\mathbf{u}\nabla T\rangle + \langle D_l(T)\rangle + \langle D_z(T)\rangle + \langle I(z)\rangle. \tag{2}$$

Averaging Eq. (2) over the long-term mean (40 years, denoted by an overline), the tendency is found negligible, therefore:

$$-\overline{\langle\mathbf{u}\nabla T\rangle} + \overline{\langle D_l(T)\rangle} + \overline{\langle D_z(T)\rangle} + \overline{\langle I(z)\rangle} \approx 0. \tag{3}$$

Using a classic Reynolds decomposition, each variable can be decomposed into a low-frequency (subscript m) and eddy (prime) part (departure from a 30-day running mean):

$$X = X_m + X'. \tag{4}$$

Note that the eddy part might still contain some variability associated with Kelvin waves. However, TIWs are dominant in this monthly frequency range. Moreover, as detailed later, the TIW effects are evaluated from the difference between TIWs-RUN and NOTIWs-RUN, therefore processes not impacted by TIWs will not affect our analysis. The advective term can be decomposed as

$$\mathbf{u}\nabla T = \mathbf{u}_m\nabla T_m + \mathbf{u}'\nabla T' + \mathbf{u}_m\nabla T' + \mathbf{u}'\nabla T_m. \tag{5}$$

Averaging Eq. (5) on the long term, it becomes

$$\overline{\mathbf{u}\nabla T} = \overline{\mathbf{u}_m\nabla T_m} + \overline{\mathbf{u}'\nabla T'}. \tag{6}$$

As the mean is a linear operation (when weighted by the right ratio), cross terms $\overline{\mathbf{u}'\nabla T_m}$ and $\overline{\mathbf{u}_m\nabla T'}$ are equivalent to $\overline{(\mathbf{u}'\nabla T_m)_m}$ and $\overline{(\mathbf{u}_m\nabla T')_m}$, which vanish by definition.

The mixing, tendency, and forcing terms were computed online by the model as monthly averages. However, for technical reasons, the advective terms were computed offline from daily average fields. These offline advection terms were compared to online advection terms obtained from a short test run of TIWs-RUN, confirming the accuracy of our estimate from daily averages. We verified the closure of the budget averaged over the first 50 m and over the 40 years: the sum of advective, mixing, and atmospheric forcing terms are close to zero, as well as the tendency term.

3. Validation of the model

In this section, we assess the control simulation (TIWs-RUN) with regards to the variety of observational products described in section 2, with a particular focus on equatorial currents and associated mesoscale activity at intraseasonal time scales, the central point of this study.

a. Validation of tracers and heat fluxes

Figure 1a shows the SST long-term mean obtained from 40 years of simulation. Consistent with the literature, the

TABLE 1. Mean values from time series used in the Taylor diagram, for the model and observations. Last line shows the model biases (i.e., model minus observations).

	SST (°C)	SSS (psu)	TD_W (m)	TD_E (m)	SW (W m^{-2})	LW (W m^{-2})	LHF (W m^{-2})	SHF (W m^{-2})
Model	26.8	35.08	154.5	71.7	262.1	−56.5	−111.6	−8.4
Observation	26.1	34.97	146.2	47.3	251.8	−47.8	−82.7	−3.9
Bias	0.7	0.11	8.3	24.4	10.3	−8.7	−28.9	−4.5

typical features of the eastern tropical Pacific can be observed as, e.g., the presence of the cold tongue, a patch of cold water along the equator that lies between 140°W and the Ecuadorian coast and extends along South America shorelines due to the Peruvian coastal upwelling. The cold tongue is flanked on each side by warmer waters, in particular in the Northern Hemisphere, where the eastern Pacific warm pool extends from the tip of Baja California to the northern edge of the cold tongue (Wang and Fiedler 2006). Contours on Fig. 1a indicate a warm bias between the model and the climatology computed from OISST that reaches 0.6°C in the equatorial band and 1.6°C in the eastern part of the cold tongue. This bias can be explained by at least two factors:

- On the one hand, from a too weak equatorial upwelling caused by a thermocline too flat along the equator as indicated by the strong bias in the simulated thermocline depth (TD_W) overestimated by 8.3 m (i.e., 5.7% of the observation) in the west, and by almost 25 m (i.e., more than 50%) in the east (TD_E) (Table 1). This could result from a poor wind stress curl representation in CFSR along with an inaccurate equatorial dynamic at the open boundaries forced with SODA v3.4.2.
- On the other hand, from a positive shortwave radiation bias of roughly 4%, which can contribute to the excessive SST warming and in turn explains the too strong latent and sensible heat flux amplitudes (−28.9 and −4.5 W m^{-2}, respectively; Table 1). The bias in shortwave fluxes is a known bias in CFSR, especially in the western part of the eastern Pacific (Wang et al. 2011). It is most likely due to the deficiency in cloudiness in CFSR (Dolinar et al. 2016). We also note a positive bias of 18.2% for the longwave radiation.

The SSS is only slightly biased as compared to observations (0.11 psu) despite the overestimation of precipitation in CFSR noted by Dolinar et al. (2016). This might result from bias compensations between too strong precipitations and evaporation related to the overestimation of latent heat fluxes.

Overall, the Taylor diagram (Taylor 2001) reveals that the model simulates accurately the eastern tropical Pacific variability, as most variables are well correlated with observations (correlations higher than 0.6) and have normalized standard deviations close to 1, indicating amplitudes similar to observational time series. The sensible heat flux (SHF), however, has a poor correlation coefficient of 0.3 and its standard deviation is 1.8 times higher than observations. Yet, this result has to be taken with caution, as fluxes observations are problematic, which might hinder an accurate representation of their variability. Indeed, a similar analysis of fluxes [SHF, latent heat flux (LHF), and shortwave radiation (SWF)] variability using the COREv2 dataset (Yeager and Large 2008) displays very contrasted results for latent and sensible heat flux. The correlation coefficient for SHF becomes slightly negative (−0.02) and the standard deviation is 1.6 times higher than observations. These results also vary spatially. For the intertropical convergence zone (ITCZ) region (2°–15°N and 180°–90°W), the normalized standard deviation of TropFlux SHF is close to 1, whereas the COREv2 SHF is 1.4. For the same region, the correlation coefficient reaches 0.5 for the TropFlux SHF, but stays under 0.3 for the COREv2 SHF, confirming the strong dependence of the results to the observational product considered (Valdivieso et al. 2017).

b. *Validation of mean circulation and mesoscale activity*

The 40-yr averaged mean zonal circulation is then compared to the drifters-derived climatology at the surface (Fig. 2a) and to Johnson's for their vertical structure (Fig. 2c). Figure 2a exhibits a good agreement with observations for both the position and intensity of the SEC and NECC. In addition, the model captures well their vertical extension at 125°W as indicated by the good match between simulated (shading) and observed (contours) zonal velocity on Fig. 2c. In particular, the SEC extends coherently poleward with its southern and northern branches centered near 3°S and 3°N, and reaching −0.3 and −0.5 m s^{-1}, respectively, the latter being slightly underestimated by 0.2 m s^{-1} in the eastern part of the basin (Fig. 2a). In addition, the SEC/NECC surface front is located at 5°N consistently with Johnson's observations. The EUC vertical structure and intensity also matches well with observations from Johnson, in particular exhibiting a similar maximum value of 0.8 m s^{-1} at the equator. The maximum value is located slightly deeper than Johnson's, which is likely due to the too weak equatorial upwelling in our simulation.

To complement this evaluation and as a preliminary diagnostic of TIW activity, the mean mesoscale activity is then assessed using the eddy kinetic energy [EKE = $(1/2)(u'^2 + v'^2)$]. Shading on Fig. 2b shows the mean simulated EKE from the control configuration (TIWs-RUN). Note that in order to compare to CMEMS, the 1993–2019 average is shown here. Consistent with the literature (Baturin and Niiler 1997; Wang et al. 2020), a strong mesoscale activity is found along the equator, spreading northward up to 5°N, a characteristic signature of TIWs. Contours show the bias between the model EKE and the EKE derived from CMEMS daily currents. The simulated EKE is overestimated by up to 100 cm^2 s^{-2} in the equatorial band. This is not surprising as the CMEMS currents contain only the geostrophic and Ekman currents. A more detailed validation of TIW characteristics in the control experiment will be performed in the next section.

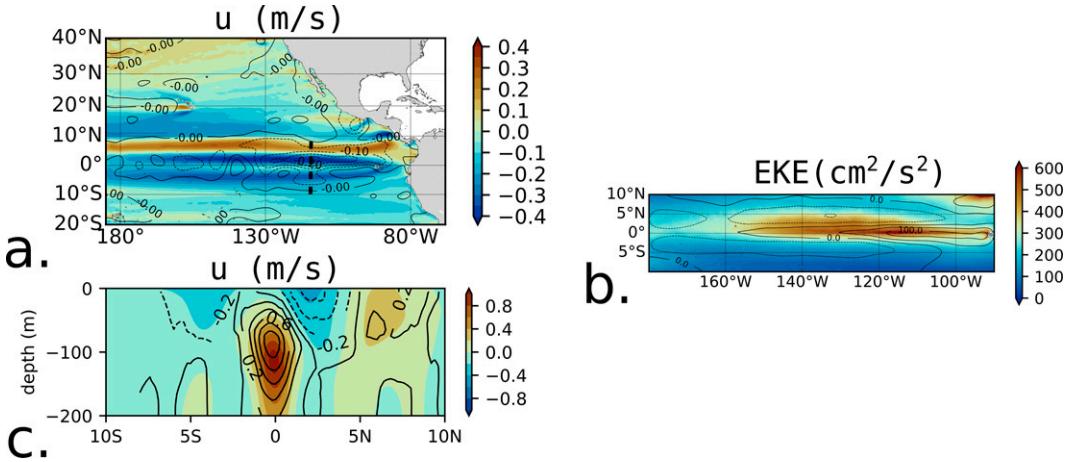

FIG. 2. Evaluation of TIWs-RUN dynamics. Maps of mean surface (a) zonal currents and (b) EKE calculated using fluctuations of horizontal currents from a 30-day running mean. Shading represents the control experiment (TIWs-RUN) mean zonal surface currents from 1980 to 2019 in (a) and mean surface EKE from 1993 to 2019 in (b). Solid and dashed contours show respectively the positive and negative mean amplitude bias between the model and the climatology obtained from the NOAA drifter database in (a) and the 1993–2019 CMEMS currents in (a). Contours are every 0.05 m s^{-1} in (a) and every 50 cm^2 s^{-2} in (b). (c) Depth–latitude section of zonal currents at 125°W [represented in dashed line in (a)] for model (shading) and observations from Johnson (contours). Eastward (westward) currents are shown with solid (dashed) lines.

Overall, despite the presence of some biases, in particular related to the zonal tilt of the equatorial thermocline, the mean state and circulation of the eastern tropical Pacific are well represented in the control configuration, which testifies to the model's ability to simulate adequately the complex equatorial dynamics (Kessler 2006). Regardless, hereafter, the control configuration is compared to a sensitivity experiment in which only the TIW activity is altered. In that sense, the aforementioned mean biases should be similar in both experiments and therefore cancel out when evaluating the specific TIW effect on the eastern tropical Pacific mean state.

4. A framework for damping TIWs in an ocean model

This section is dedicated to describing and validating the methodology employed to smooth out TIWs in the sensitivity experiment (NOTIWs-RUN).

a. *TIW characteristics and associated mesoscale activity in TIWs-RUN*

TIWs have a clear and spatially coherent signature between surface meridional velocity and temperature intraseasonal anomalies, as indicated by snapshots taken during the boreal winter of a La Niña year (i.e., both extremely TIW active periods) (Figs. 3a,b). In particular, we observe alternating positive and negative velocity anomalies localized in the equatorial band (Fig. 3a) and around which filaments of SST anomalies are seen to meander (Fig. 3b). This TIW-induced mesoscale activity is then assessed by calculating the intraseasonal EKE. The highest values of EKE are found along the equator, spreading northward with a maximum at 1°N (Fig. 2b), the region where TIWs are the most active. In addition, EKE is found to be strong (250–500 cm^2 s^{-2}) within the first 100 m (Fig. 3c) and drop to almost zero below 200 m.

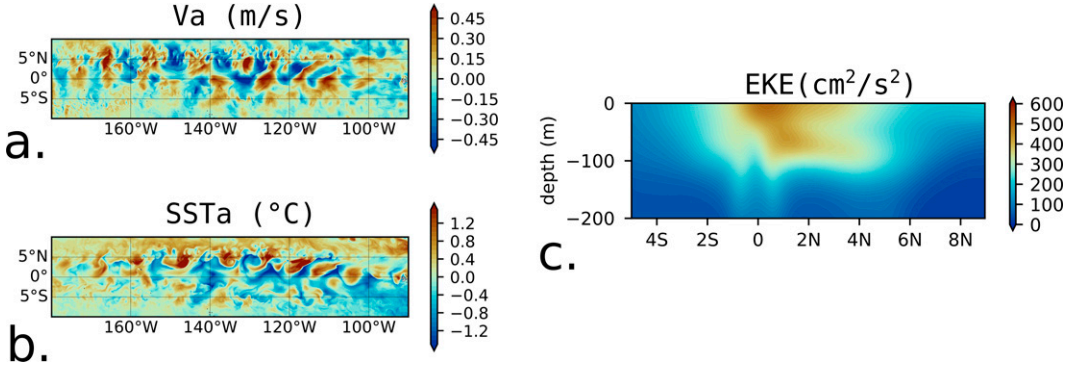

FIG. 3. Illustration of TIW activity. Snapshots (31 Dec 2017) of (a) surface meridional velocity anomaly (m s^{-1}) and (b) surface temperature anomaly (°C), and (c) meridional section of EKE (cm^2 s^{-2}) averaged between 160° and 100°W.

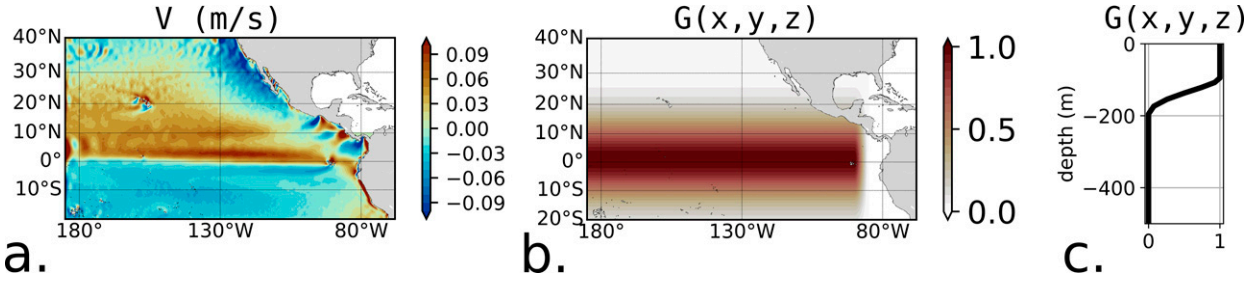

FIG. 4. Damping framework. (a) Meridional current annual climatology in the control experiment (TIWs-RUN). (b) Horizontal and (c) vertical structure of the nudging geometry $G(x, y, z)$.

These diagnostics allow delineating the spatial (including vertical) region of prominent TIW-induced mesoscale activity.

b. *Damping methodology*

To smooth out the TIWs without affecting other processes in NOTIWs-RUN, the mixed layer meridional currents v in the active TIW region (see Fig. 4) are nudged toward the monthly climatology v_0 derived from TIWs-RUN as such:

$$\frac{dv}{dt} = f(v) + G(x, y, z)\frac{v_0(t) - v(t)}{\tau}. \quad (7)$$

The left-hand part of the equation is the temporal evolution of v. The first term of the right-hand part $f(v)$ represents the evolution of v due to advection–diffusion processes. The last term of the right-hand side represents the nudging of v toward the monthly climatology v_0, computed from the control experiment (TIWs-RUN) and which does not display much trace of the TIW mesoscale features (see Fig. 4a for the annual climatology of the surface v field). Yet, the Ekman divergence at the equator is still present, indicating that the nudging of v toward v_0 is expected to damp TIW activity while keeping the mean dynamics intact. The nudging time scale τ is set to 5 days, so that both TIW modes with periods near 33 and 17 days, and commonly referred to as the Rossby and Yanai modes (Lyman et al. 2007; Wang et al. 2020), are effectively removed.

Based upon the TIW spatial features discussed above (see section 4a), the nudging geometry is restricted to the prominent region of TIW activity by applying a spatial Gaussian function $G(x, y, z)$ (see Fig. 4 and the appendix for details). This function maximizes the nudging along 1°N and reduces it poleward with a decreasing meridional rate of 10° (Fig. 4b). It is deactivated between the Galapagos Island and the coast to preserve submesoscale features in the coastal area for instance related to filaments breaking loose from the Humboldt upwelling system. Even though TIWs have been shown to radiate internal waves downward (Jing et al. 2014; Holmes and Thomas 2016; Tanaka and Hibiya 2019; Delpech et al. 2020), the nudging is concentrated within the first 200 m below the surface (Fig. 4c) where TIWs are mostly generated and active (Fig. 3d).

Note that only meridional currents are nudged. This allows an effective damping of the development of TIWs due to their strong signature in v, while keeping equatorial Kelvin waves mostly untouched, as their meridional structure in the long-wave approximation of shallow water equations is null at the equator (Cane and Sarachik 1977). Therefore, the nudging of meridional velocity only is expected to preserve the important role played by Kelvin waves in the equatorial dynamics, for instance related to the kickstarting of El Niño events (e.g., McPhaden and Yu 1999; Gushchina and Dewitte 2012). By nudging the meridional currents, the other dynamical and tracer components are expected to adjust and vanish as well.

c. *Validation of damping efficiency*

To validate to which extent the damping methodology allows smoothing out TIW variability, we first compare EKE between the NOTIWs-RUN (Fig. 5) and TIWs-RUN (Figs. 2b and 3c). These figures indicate an EKE (and associated mesoscale activity) decrease of almost 50% in the TIW active region. When separating the EKE into u'^2 and v'^2 parts reconstructed using the five first complex empirical orthogonal function (CEOF) modes (i.e., accounting together for most of the TIWs variability, see below for more details on the CEOF analysis), we observe a reduction of u'^2 and v'^2 from TIWs-RUN to NOTIWs-RUN of 62% and 94%, respectively, indicating that the remaining mesoscale activity in NOTIWs-RUN is for the most part not due to TIWs but

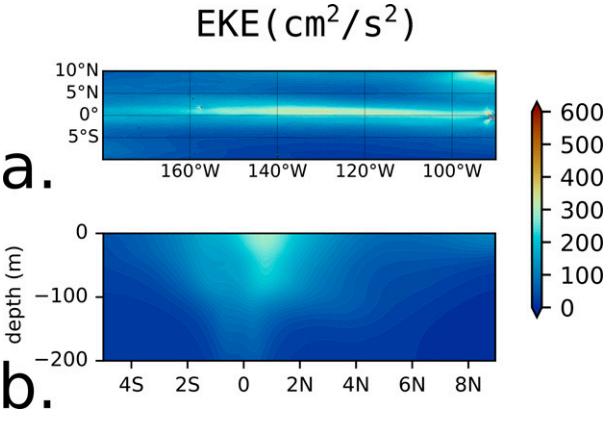

FIG. 5. EKE ($cm^2\ s^{-2}$) in NOTIWs-RUN (a) averaged over 200 m and (b) meridional section averaged between 160° and 100°W.

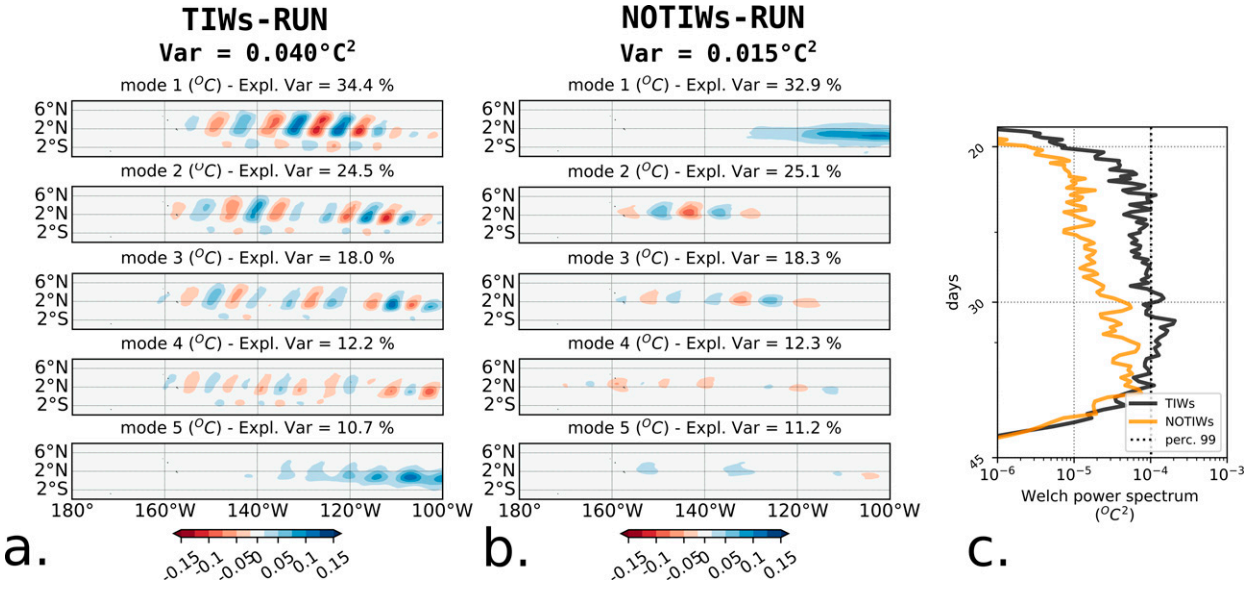

FIG. 6. First five modes' real part of the complex empirical orthogonal function (CEOF) decomposition of 20–40 days bandpassed SST anomalies performed in the TIW active region (4°S–8°N, 180°–100°W) for (a) the TIWs-RUN and (b) the NOTIWs-RUN. (c) Mean Welch power spectrum of the reconstructed SST anomaly field over maximum CEOF signal area (4°S–8°N, 140°–100°W) for each simulation using the first four CEOF modes.

instead most likely due to wind-driven currents (not shown). This also confirms the coherent adjustment of zonal currents at TIW scale to our nudging procedure applied only on v.

To investigate the TIW damping efficiency in more detail, CEOFs are estimated using the 20–40 days bandpassed SST anomaly in the TIW active region (4°S–8°N, 180°–100°W) for both simulations. CEOFs (Barnett 1983) are an efficient and extensively used way to extract the spatiotemporal characteristics of TIW intraseasonal variability, as this analysis provides both amplitude and phase information and is therefore well adapted to capture waves propagation and variability (Boucharel et al. 2013, 2016; Xue et al. 2021; Escobar-Franco et al. 2022).

The first five dominant modes are shown in Fig. 6a for TIWs-RUN and in Fig. 6b for NOTIWs-RUN. The fifth mode of TIWs-RUN and the first mode of NOTIWs-RUN could correspond to SST variations associated with the intraseasonal Madden–Julian oscillation (Madden and Julian 1994), as found by Maloney and Kiehl (2002). Similar to their results, the phase of this mode (not shown) indicates a northward propagation and seems to correspond to a potential interaction of this mode with TIWs in the TIWs-RUN, but this is beyond the scope of this paper. In the TIWs-RUN (Fig. 6a), modes 1–4 are associated with TIW variability as indicated by the alternating positive and negative nodes located between 2°S and 6°N. They are characterized by high explained variances of 34.4%, 24.5%, 18.0%, and 12.2%, respectively.

In the NOTIWs-RUN (Fig. 6b), modes 2–4 exhibit patterns resembling TIW variability, yet with small explained variances. Moreover, the total variance of the NOTIWs-RUN signal is 63% lower than that of the TIWs-RUN (standard deviation of 0.015° vs 0.04°C^2), giving even less weight to these modes of variability, and indicating that TIWs have been strongly damped in the NOTIWs-RUN sensitivity experiment. This is confirmed by the large decrease in power spectra (reconstructed using the first four CEOF modes and averaged in the TIW active region) in the TIW typical period range of 17–33 days between the two experiments (Fig. 6c).

For a more visual assessment of the efficiency of our method, we then show Hovmöller diagrams of the 20–40 days bandpassed zonal SST anomaly averaged between 2° and 5°N for TIWs-RUN in Fig. 7a and NOTIWs-RUN in Fig. 7b during the strong La Niña episodes of 2017 and 2018, i.e., periods favorable to TIW development as explained in the introduction section. In the TIWs-RUN (Fig. 7a), a strong TIW activity is observed during the boreal autumn of both years, whereas the 2015/16 winter marked by a strong El Niño event does not exhibit, as expected, any sign of TIW propagation. In contrast, in the NOTIWs-RUN (Fig. 7b), TIWs have almost fully disappeared during all three winters, indicating that their development has been effectively prevented by the nudging procedure. These results are valid throughout the entire 40-yr period.

Finally, to establish that other aspects of the equatorial dynamics, in particular related to Kelvin waves propagation, are left unaltered by our methodology, Hovmöller diagrams of the 60–130 days bandpassed thermocline depth anomaly averaged between 2°S and 2°N for TIWs-RUN and NOTIWs-RUN are shown in Figs. 7c and 7d, respectively. In both simulations, one can identify the presence of Kelvin waves by their eastward propagating signal at a phase speed of 2.3 m s^{-1}.

To sum up, the nudging procedure applied in NOTIWs-RUN effectively damps TIW activity while keeping the important Kelvin waves signal in this region untouched. Consequently,

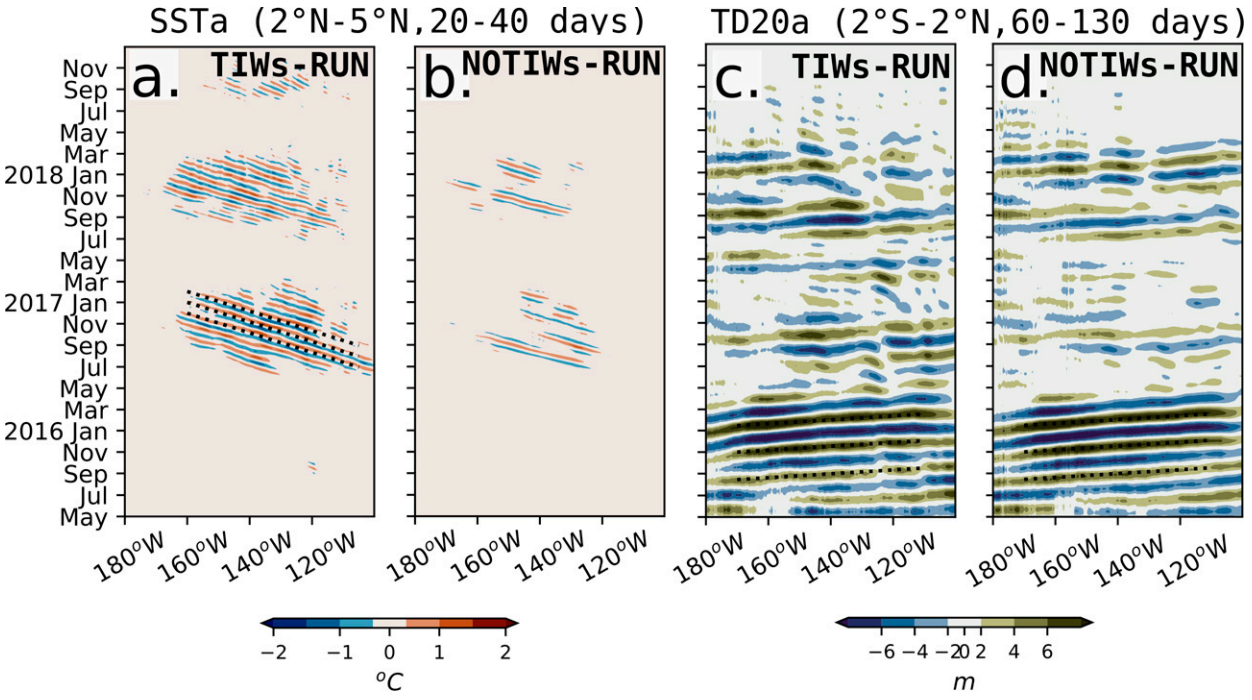

FIG. 7. Hovmöller diagrams of the 20–40 days bandpassed zonal SST anomalies averaged between 2° and 5°N for (a) TIWs-RUN and (b) NOTIWs-RUN between May 2015 and December 2017. Dotted lines represent the westward propagation at a 0.46 m s^{-1} phase speed. (c),(d) As in (a) and (b), but for the 20°C thermocline depth anomaly averaged in the 2°S–2°N latitudinal band and bandpassed between 60 and 130 days (i.e., the Kelvin waves dominant period range) for TIWs-RUN in (c) and NOTIWs-RUN in (d). Dotted lines represent the eastward propagation at a 2.3 m s^{-1} phase speed.

the differences observed between the two sensitivity experiments, which have the very same horizontal and vertical resolutions, will most likely originate from TIW-induced effects only.

5. TIW effects on the eastern tropical Pacific Ocean

The aim of this section is to investigate to which extent TIW activity alters the oceanic mean state. To do so and hereafter, TIW impacts will be assessed by subtracting NOTIWs-RUN to TIWs-RUN.

a. *Effects on the oceanic mean state*

TIW effects on mean temperature and circulation are shown in Fig. 8. At the surface, TIWs warm up the cold tongue by up to 0.4°C and cool down the surrounding waters by the same amount (Fig. 8a). In depth, the warming of the cold tongue spreads down to 150 m with a maximum of 0.50°C at 100 m while the cooling of southern and northern waters is constrained to the first 50 and 100 m, respectively (Fig. 8b).

The comparison between the two simulations also reveals a significant impact of TIWs on mean zonal and meridional currents amplitude (Figs. 8c,d), with an overall decrease of zonal currents intensity. In particular, at the subsurface, the eastward EUC is significantly reduced (by up to −0.20 m s^{-1} near the surface and −0.12 m s^{-1} in the core, i.e., more than 15%) and its upper limit is deepened from the surface to 25 m. The intensity of both the westward SEC located at the surface between 5°S and 3°N and NECC located near 7°N are also strongly reduced by −0.13 m s^{-1} (30%) and −0.06 m s^{-1} (20%), respectively. In contrast, TIWs lead to a slight increase of the equatorial Ekman divergence (oriented poleward in surface and equatorward in depth) in particular in the Northern Hemisphere by 0.02 m s^{-1} (20%) and 0.01 m s^{-1} (20%), as shown by the red shadings between 2° and 4°N, respectively.

b. *Energy exchange between oceanic mean state and TIWs*

As detailed by many others before (e.g., Qiao and Weisberg 1998; Masina and Philander 1999; Xue et al. 2021), the time evolution of long-term averaged EKE depends on the baroclinic (P_eK_e) and barotropic (K_mK_e) conversion rates, which are

$$P_eK_e = -\frac{g}{\rho_0}\overline{w'\rho'}, \tag{8}$$

$$K_mK_e = -[\overline{u'u'}\partial_x\overline{u} + \overline{u'v'}\partial_y\overline{u} + \overline{u'w'}\partial_z\overline{u} + \overline{u'v'}\partial_x\overline{v} + \overline{v'v'}\partial_y\overline{v} + \overline{v'w'}\partial_z\overline{v}] \simeq -\overline{u'v'}\partial_y\overline{u}, \tag{9}$$

where $g = 9.81$ m s^{-2} is the gravitational acceleration constant and $\rho_0 = 1025$ kg m^{-3}.

The spatial distributions of K_mK_e and P_eK_e, which represent the energy exchange from the mean kinetic energy and from the eddy available potential energy to the EKE, are

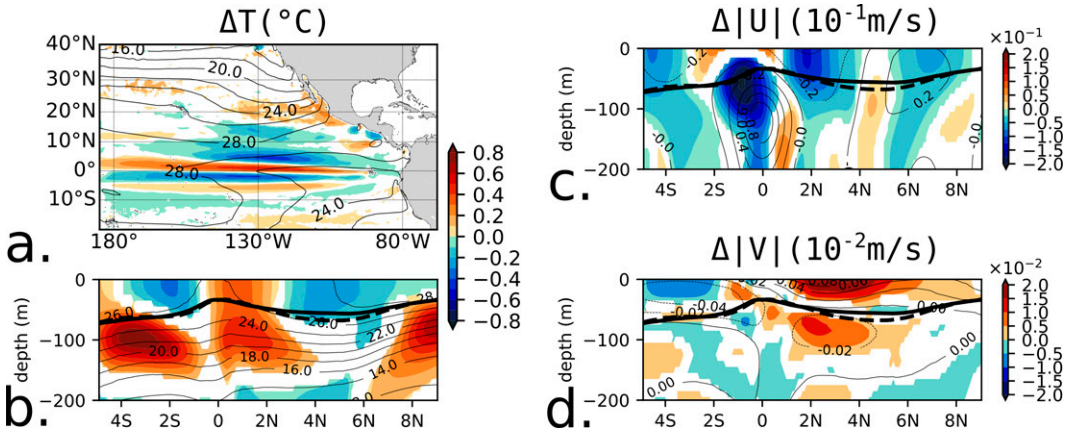

FIG. 8. Mean state differences between TIWs-RUN and NOTIWs-RUN for (a) sea surface temperature, (b) vertical section of temperature, (c) amplitude of zonal, and (d) meridional currents. Depth–latitude sections are averaged between 160° and 100°W. Only differences significant at the 99% confidence level (i.e., p value of the two-tailed Student's t test below 0.01) are displayed. Contours (every 2°C) show the mean values of temperature in the TIWs-RUN in (a) and (b), U every 0.2 m s^{-1} in (c), and V every 0.02 m s^{-1} interval (solid lines for positive and dashed lines for negative values) in (d). Thick black (dashed) line in (b)–(d) shows the mean mixed layer depth in TIWs-RUN (NOTIWs-RUN).

shown in contours in Fig. 9. Only the dominant barotropic term $-\overline{u'v'}\partial_y\overline{u}$ is shown here. Both are essentially positive (solid contours) and are increased when TIWs are present (indicated by the red shading), in particular in a zonal band north of the equator and over the first 100-m depth, indicating a source of EKE in the TIW region. The strong meridional gradient and weak stratification lead to large baroclinic conversion (Masina and Philander 1999), and the strong meridional shear of zonal currents, especially between the EUC and the northern branch of the SEC, leads to high barotropic conversion.

To complement this analysis, the rate of kinetic energy transfer across spatial scales is shown in Fig. 10 (for details on the computation, see, for instance, Marchesiello et al. 2011; Renault et al. 2019), where positive (negative) energy rates mean a transfer toward smaller (larger) scales. From 500 km to smaller scales, both experiments are characterized by a forward cascade of energy, i.e., a transfer of energy from the larger scales toward the smaller scales, which can be interpreted as the signature of submesoscale mixed layer eddies with scales of 50–200 km that form along TIW fronts as suggested by Marchesiello et al. (2011). The KE-flux spectrum at TIW scales (≈1000 km) displays negative transfer rates in the TIWs-RUN (black line) but positive values in the NOTIWs-RUN (orange line), indicating that TIWs are responsible for an inverse energy cascade, i.e., a transfer of energy from the TIWs to the larger-scale currents. This reveals a rectified effect of the TIWs onto the larger scale associated with the eastern tropical Pacific mean circulation. To sum up, this energy analysis confirms that TIWs play a central role in the energy budget of this region by in particular 1) harvesting energy from temperature meridional gradient through baroclinic instability, and from the meridional shear of currents through barotropic instability, therefore acting to reduce the mean zonal circulation,

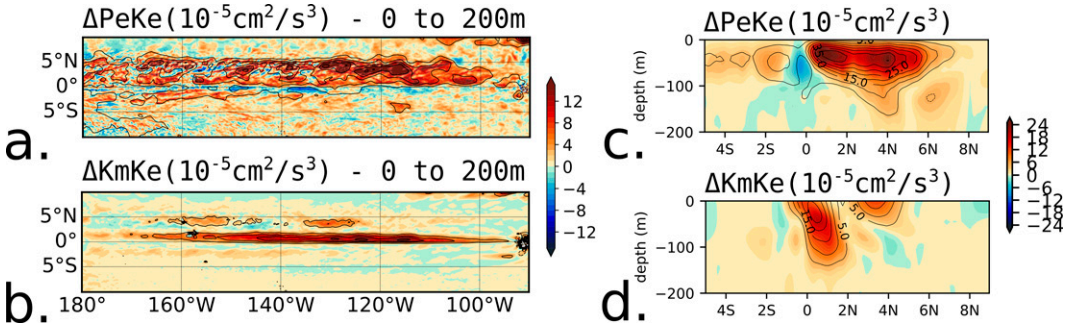

FIG. 9. Mean differences between TIWs-RUN and NOTIWs-RUN for (a),(c) baroclinic (P_eK_e) and (b),(d) dominant barotropic ($K_mK_e \simeq -\overline{u'v'}\partial_y\overline{u}$) conversion rates ($10^{-5}$ cm^2 s^{-3}). (left) Maps of conversion rates averaged over the first 200 m. (right) Depth–latitude sections averaged over 160°–100°W. Contours show the mean values of conversion rates in the TIWs-RUN every 5×10^{-5} cm^2 s^{-3} (solid lines for positive and dashed lines for negative values). A Gaussian smoothing of 1° radius was applied for maps in (b)–(d) and 5° radius for (a).

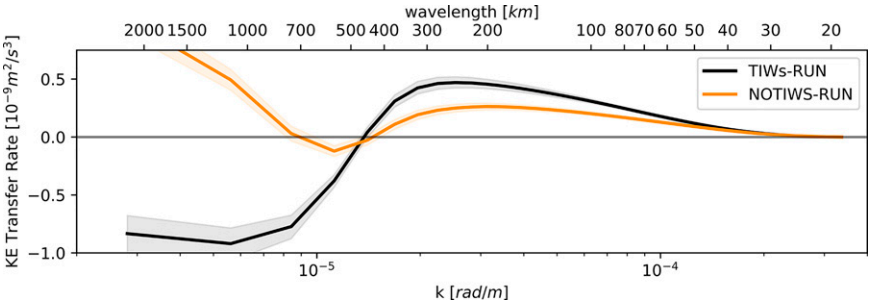

FIG. 10. Spectrum of KE transfer rate averaged between (160°–100°W, 10°S–10°N) and from surface to 50-m depth. Surfaces show the 95% confidence interval from a bootstrap method on annual averages (see section 2d).

and 2) injecting energy back into the larger scales through an inverse energy cascade responsible for a rectified effect onto the mean state.

c. *Quantification of direct and rectified effects of TIWs from a heat budget analysis*

To evaluate the mechanisms responsible for the direct and rectified effects of the TIWs onto the mean state, a heat budget is derived in both simulations. Additionally, to make a better physical sense of the TIW effects on the eastern Pacific mean state, the advection of temperature is separated into a mean and a fluctuating part through a Reynolds decomposition (see section 2e). The difference in the anomalous and mean advection terms between the two experiments will allow quantifying the TIW direct and rectified effects on the eastern tropical Pacific mean state.

The difference in the heat budget vertical structure averaged over 160°–100°W between the two simulations is presented in Fig. 11. The top panels represent the total advection, horizontal and vertical mixing (the horizontal term being negligible), and heating by atmospheric forcing terms. The other panels represent the decomposition of the advective terms into zonal, meridional, and vertical parts, and into total (X), mean (X_m), and fluctuating (X') parts.

At the surface, a compensating effect between mixing and heating by atmospheric forcing is observed with TIWs warming up the 0°–2°N band and cooling down the surrounding waters through mixing (Fig. 11b), while the forcing term exhibits

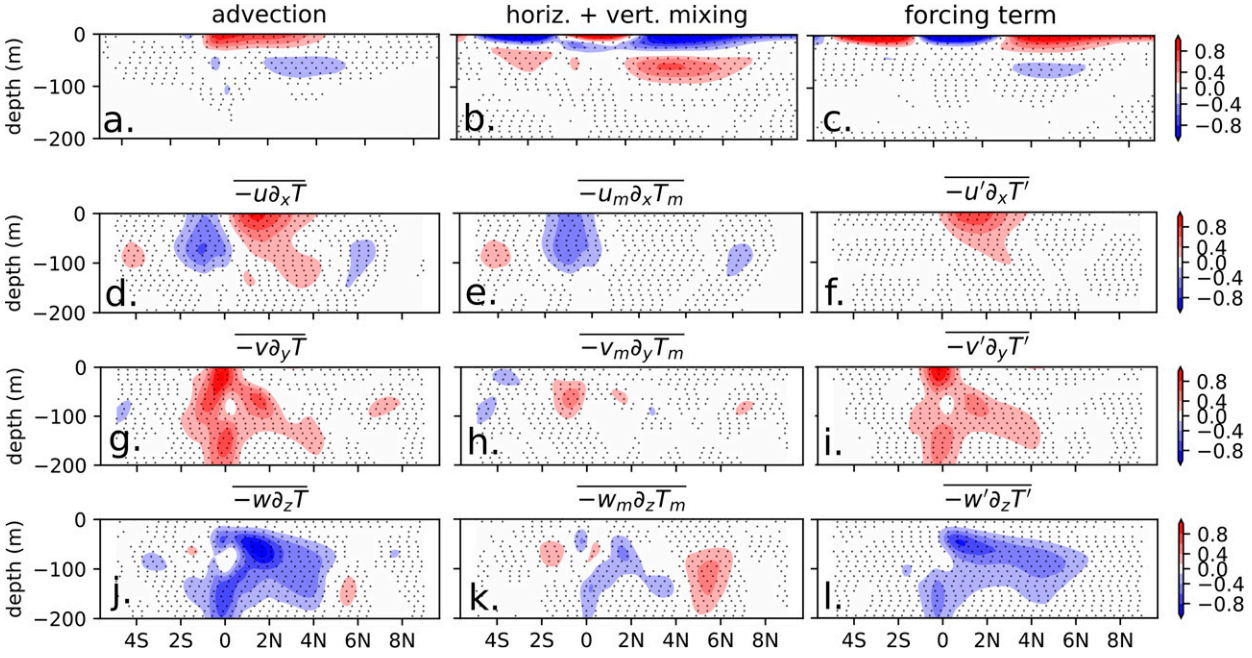

FIG. 11. Depth–latitude sections of TIW contribution to heat budget terms (i.e., TIWs-RUN minus NOTIWs-RUN; °C month^{-1}), averaged over 100°–160°W and over 40 years. Top three panels show the total (a) heat advection, (b) heat mixing, and (c) heating by atmospheric forcing terms. Other panels show the (d)–(f) zonal, (g)–(i) meridional, and (j)–(l) vertical terms of heat advection, decomposed into total parts in (d), (g), and (l); mean parts in (e), (h), and (k); and fluctuating parts in (f), (i), and (l). Dots show significant differences at the 99% confidence level (i.e., p value of the two-tailed Student's t test below 0.01).

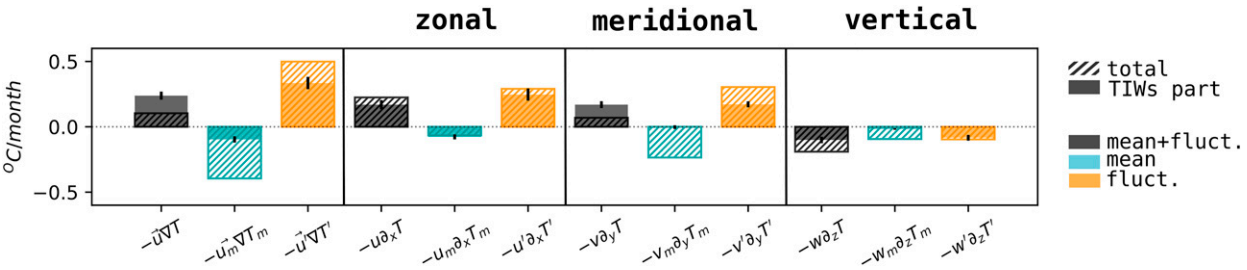

FIG. 12. Total (hatched) and residual heat advection (TIWs-RUN minus NOTIWs-RUN, plain color) averaged over 2°S–6°N and 160°–100°W, in the first 50 m. Black bars represent the total advection terms, blue bars the mean advection terms, and orange bars the fluctuating advection terms. Error bars stand for the ±1/2 annual standard deviation.

an opposite behavior (Fig. 11c). Yet, our approach does not allow assessing properly the effect of TIWs on atmospheric fluxes as the atmospheric forcing is prescribed. In the subsurface (between 50 and 100 m) TIWs tend to warm up northern waters through vertical mixing.

The overall TIW-induced advection leads to a warming of the 0°–4°N band, with a peak value of 0.8°C month^{-1} (Fig. 11a). The zonal component of TIW advection (Fig. 11d) is separated into a cooling over 2°S–0° through mean advection (i.e., rectified effect, Fig. 11e) and a warming over 0°–4°N through fluctuating advection (i.e., direct effect, Fig. 11f). The location of cooling by mean zonal advection is consistent with the weakening and deepening of the EUC by TIWs (Fig. 8c). As the presence of TIWs leads to a significant EUC weakening, less warm waters can be advected from the central-western Pacific, which could explain this cooling rectified effect. The meridional component of TIW advection (Fig. 11g) is almost fully explained by the warming through fluctuating meridional advection (Fig. 11i), which spreads from the surface to 200 m. In surface, it is constrained to the equatorial region (1°S–1°N) while it extends more meridionally with depth (2°S–4°N). The vertical component of TIW advection (Fig. 11j) cools down the 2°S–5°N band, from subsurface to 200 m. It is mostly due to fluctuating vertical advection (Fig. 11l), with only a small portion due to mean vertical advection (Fig. 11k). This highlights a complex interplay between potential changes in the upwelling/downwelling velocities and vertical temperature gradients. Unsurprisingly, the fluctuating part (i.e., the direct effect of TIWs) is found to be the largest near the surface concurrently with the large zonal and meridional fluctuating terms associated with the very strong zonal current shear (Fig. 8c) and meridional temperature gradient (Fig. 8b) concentrated in the mixed layer. The fluctuating vertical advection is constrained deeper, below the mixed layer, as found in Menkes et al. (2006).

The advection contribution to the heat budget averaged over the first 50 m and the cold tongue area (160°–100°W, 2°S–6°N) is shown in Fig. 12. This large band in latitude has been selected to be consistent with other studies such as Menkes et al. (2006). However, it should be kept in mind that there are latitudinal changes of advective components (in particular, the zonal component) within this band. The advection (gray bars) is decomposed into mean (blue) and fluctuating (orange) contributions. Hatched bars show the total value for TIWs-RUN, while plain color bars show the part due to TIWs (i.e., TIWs-RUN minus NOTIWs-RUN). Each term is decomposed into zonal, meridional, and vertical parts.

The total advection warms up the cold tongue by 0.10°C month^{-1} (hatched gray, $-\mathbf{u}\nabla T$). TIW contribution to this total advection is a warming by 0.24°C month^{-1} (plain gray, same term).

The fluctuating part leads to an overall net warming of the cold tongue by 0.50°C month^{-1} (hatched orange), 68% of which being attributed to TIW activity (plain orange). This direct TIW effect warms up the cold tongue via zonal (0.25°C month^{-1}) and meridional advection (0.17°C month^{-1}), and slightly cools it down through vertical advection (−0.08°C month^{-1}), resulting in a net warming by 0.34°C month^{-1}, which is consistent with previous studies (e.g., Menkes et al. 2006; Im et al. 2012; Graham 2014) yet a bit lower than in Menkes et al. (2006), for instance. While Menkes et al. (2006) used a simple Reynolds decomposition and attribute all the fluctuating part to the TIWs, other mesoscale processes might remain included in their analysis. The mechanisms leading to the TIWs-induced warming are explained in detail in Menkes et al. (2006) (see their Fig. 6 for a detailed sketch).

Advection by the mean flow cools down the cold tongue by 0.40°C month^{-1} (hatched blue in terms $-\mathbf{u}_m\nabla T_m$). As found in previous studies (e.g., Menkes et al. 2006) and in our data (not shown), it is a balance between the vertical advection (cooling in the equatorial upwelling and warming in the downwelling areas), meridional advection (Ekman divergence at the surface exporting cold water outside the cold tongue, and convergence in depth importing warm waters), and zonal advection (EUC bringing western warm waters in the cold tongue, SEC bringing eastern cold waters to a lesser extent). On average, the mean advection results in a cooling of the cold tongue through a subtle balance between currents and temperature gradients. Twenty-five percent of this cooling is attributed to the TIW rectified effect (−0.10°C month^{-1}, plain blue).

To summarize, on average, TIWs tend to warm up the cold tongue by 0.34°C month^{-1} through direct anomalous zonal and meridional heat advection, while their rectified effect leads to cooling by −0.10°C month^{-1} due to a reduction of mean zonal advection most likely associated with a significant weakening and deepening of the EUC. The combined TIW effects result in a net cold tongue warming by 0.24°C month^{-1}.

6. Summary and discussion

In this study, a new framework is introduced to isolate and quantify impacts of TIWs on the eastern tropical Pacific Ocean background state in a regional ocean model. This methodology is based upon the comparison between two eddy-rich sensitivity experiments, one (TIWs-RUN) reproducing realistically the regional mean state and circulation, as well as the essential TIW dynamics, and the other (NOTIWs-RUN) is identical but TIWs are damped online by nudging the meridional velocities toward their monthly climatology obtained from the TIWs-RUN. This method effectively prevents TIWs from growing and propagating, while keeping the rest of the equatorial dynamics and in particular Kelvin waves, a key dynamical feature of this region, unaltered.

By subtracting TIWs-RUN from NOTIWs-RUN, differences can mainly be attributed to TIW variability and can then be evidenced and quantified. In particular, two pathways are identified as source of changes: 1) a direct way, i.e., through TIW-induced mesoscale dynamics, and 2) a rectified way, i.e., through upscaling feedbacks from TIW variability back onto the mean state and circulation. On the one hand, TIWs are shown to pump up energy from the mean shear of zonal currents through barotropic conversion, which reduces the mean zonal circulation and in particular decreases the speed of the SEC, EUC, and NECC, respectively, by up to 30%, 15%, and 20%. On the other hand, this effect is also partly balanced by a reinjection of energy from TIWs back into the larger scales through an inverse energy cascade. Moreover, TIW activity is shown to reduce the meridional temperature gradient in the mixed layer, which tends to warm up the cold tongue and cool down surrounding warmer waters by up to 0.4°C on average.

To investigate the main physical processes behind this dual energy cascade, a heat budget has been derived in both simulations. A classic Reynolds decomposition, i.e., into mean and fluctuating terms, and their differences between the two sensitivity experiments allow disentangling and quantifying properly the TIW direct versus rectified effects. Overall, the anomalous fluctuations induced by TIW mesoscale and intraseasonal variability are shown to advect heat into the cold tongue at a rate of 0.34°C month^{-1}. A rectified effect of TIWs on the background state counterbalance this warming through the reduction of mean heat advection by −0.10°C month^{-1}. In total, TIWs are responsible for an advection of warm waters into the cold tongue of 0.24°C month^{-1}. The vertical advection of heat by TIWs is mainly located below the mixed layer, with a strong direct advection of cold waters.

Because TIWs are shown to strongly affect advection, their effect on the different components has been investigated in detail. This reveals that zonal and meridional eddy advection induce a warming of the cold tongue, which is in agreement with the literature (e.g., Kessler et al. 1998; Swenson and Hansen 1999; Jochum and Murtugudde 2006; Jochum et al. 2007; Menkes et al. 2006; Graham 2014). The rectified effect operates mostly via the reduction of mean zonal advection most likely associated with a significant decrease in the amplitude of the EUC.

Other components of the budget equations are also shown to play a not-so-insignificant role. In particular, in surface, TIW induced vertical mixing is responsible for a warming of the 0°–2°N band and a cooling of other surface waters. In depth (50–100 m), TIW-induced vertical mixing warms up the waters (Fig. 11b). Several studies have focus on the potential implication of TIWs in the modulation of vertical mixing (e.g., Lien et al. 2008; Moum et al. 2009; Holmes and Thomas 2015; Inoue et al. 2012, 2019; Cherian et al. 2021). From shipboard profiling measurements of turbulence kinetic-energy dissipation rate during an active TIW period at the equator, Moum et al. (2009) have revealed an important mixing rate induced by TIWs, leading to a cooling of the surface of 1°–2°C month^{-1}. Similarly, in an idealized 1D model, Holmes and Thomas (2015) have found a 0.6°C month^{-1} cooling of the surface due to the increase of turbulent heat fluxes by TIWs. This increase of turbulent heat flux is thought to be forced by an increased shear of the EUC due to TIWs. Recently, Cherian et al. (2021) used a 1/20° regional model of the cold tongue to demonstrate that the same mechanism takes place off-equator, in the TIW cold cusps. From an oceanic model, Menkes et al. (2006) also found an enhanced diffusivity in the cold cusps, and a reduced one in warm TIW areas, and their climatological heat budget of the cold tongue reveals a positive eddy mixing flux of 0.37°C month^{-1}. However, it should be stressed that in some studies such as Moum et al. (2009) and Wei et al. (2019), the atmospheric forcing is included in the vertical mixing term as its boundary condition in surface. In our study and others (e.g., Menkes et al. 2006; Graham 2014), the atmospheric forcing is an independent term, and the boundary condition of the vertical mixing rather depends on the wind stress. Regardless, the climatological effect of TIWs on the mixing part of the heat budget is thus still debated, and the present study tends to show a complex effect of TIW induced mixing with respect to depth and latitude. This mixing could have important implications on the oceanic biogeochemistry in this key region for the carbon cycle.

Using a forced ocean model enables us to quantify the oceanic response to changes in TIW activity. However, this approach has some limitations. In particular, using a regional forced oceanic model signifies that TIW imprint is still present in the atmospheric forcing (e.g., Seo et al. 2007; Small et al. 2009), which evidently leads to a discrepancy between the ocean state and the overlaying atmosphere.

Some studies have looked at the implication of TIWs in the ENSO asymmetry (i.e., stronger El Niños than La Niñas) (e.g., An 2008; Imada and Kimoto 2012; Graham 2014). The framework presented in this paper is an effective tool to diagnose the potential rectifying effect of TIWs onto ENSO, and to a larger extent on the seasonal and interannual variability of the climate of the eastern Pacific region. However, if Kelvin waves are kept untouched here, equatorial Rossby waves may have been impacted. As suggested by Bosc and Delcroix (2008), Rossby waves could participate to the recharge–discharge oscillator paradigm of ENSO dynamics, based on meridional advection of heat between equatorial and off-equatorial regions (Jin 1997a,b). Moreover, the atmospheric feedback is needed to accurately depict the ENSO coupled phenomenon and the interannual climate of the region. This is

a strong incentive to 1) use a coupled atmosphere–ocean regional model so that the atmosphere can react in a direct and rectified way to TIW variability, and 2) fine-tune the nudging framework to keep off-equatorial Rossby waves dynamics as unaltered as possible while efficiently removing TIWs. This work is ongoing and will be the purpose of a future study.

Acknowledgments. This project was supported by the French Agence Nationale de la Recherche project MOPGA "TROCODYN" (Grant ANR-17-MPGA-0018), the CNES TOSCA I-CASCADE and CARAMBA projects, and the MUSIC project funded by the Thomas Jefferson Fund of the FACE foundation and the Embassy of France in the United States. The authors would like to acknowledge the region Occitanie and the CALMIP center for providing access to their supercomputer Olympe. We would also like to thank two anonymous reviewers for their constructive comments.

Data availability statement. All presented data are available at https://doi.org/10.6084/m9.figshare.17129588. CFSR dataset: rda.ucar.edu/datasets/ds093.1. CFSv2 dataset: rda.ucar.edu/datasets/ds094.1. Johnson's climatology of currents: https://floats.pmel.noaa.gov/gregory-c-johnson-home-page. NOAA drifter-database: https://www.aoml.noaa.gov/phod/gdp/mean_velocity.php. NOAA Optimal Interpolation of SST version 2: https://www.emc.ncep.noaa.gov/research/cmb/sst_analysis/. SODA3.4.2 reanalysis: https://www2.atmos.umd.edu/%7Eocean/index_files/soda3.4.2_mn_download_b.htm. TropFlux products: https://incois.gov.in/tropflux/. COREv2 products: https://rda.ucar.edu/datasets/ds260.2/. CMEMS surface currents https://resources.marine.copernicus.eu/product-detail/MULTIOBS_GLO_PHY_REP_015_004/.

APPENDIX

Spatial Filter *G* for Nudging

The nudging is restrained to the TIW active region by applying a space-dependent function $G(x, y, z)$ to the nudging. It can be decomposed into individual functions of depth $J(z)$, longitude $H(x)$, and latitude $I(y)$:

$$G(x,y,z) = H(x)I(y)J(z). \tag{A1}$$

Depth $J(z)$ equals one from the surface down to z_1 = 100-m depth, then smoothly decreases and reaches zero at z_2 = 200-m depth and below (see Fig. 4c):

$$J(z) = \begin{cases} 1, & \text{if } z \le z1 \\ 3\left(\dfrac{z - z_2}{z_1 - z_2}\right)^2 - 2\left(\dfrac{z - z_2}{z_1 - z_2}\right)^3, & \text{if } z_1 \le z \le z_2. \\ 0, & \text{if } z \ge z_2 \end{cases} \tag{A2}$$

Longitude $H(x)$ equals one from the most western part of the region to x_1 = 90°W, then smoothly decreases and reaches zero at x_2 = 85°W and after:

$$H(x) = \begin{cases} 1, & \text{if } x \le x_1 \\ 3\left(\dfrac{x - x_2}{x_1 - x_2}\right)^2 - 2\left(\dfrac{x - x_2}{x_1 - x_2}\right)^3, & \text{if } x_1 \le x \le x_2. \\ 0, & \text{if } x \ge x_2 \end{cases} \tag{A3}$$

Latitude $I(y)$, given by Eq. (A4), is a Gaussian centered at μ = 1°N, with a standard deviation of σ = 10° latitude;

$$I(y) = \exp\left[-\frac{1}{2}\left(\frac{y - \mu}{\sigma}\right)^2\right]. \tag{A4}$$

Figure 4b shows the combination of these two functions $H(x) \times I(y)$.

REFERENCES

An, S.-I., 2008: Interannual variations of the tropical ocean instability wave and ENSO. *J. Climate*, **21**, 3680–3686, https://doi.org/10.1175/2008JCLI1701.1.

Barnett, T. P., 1983: Interaction of the monsoon and Pacific trade wind system at interannual time scales Part I: The equatorial zone. *Mon. Wea. Rev.*, **111**, 756–773, https://doi.org/10.1175/1520-0493(1983)111<0756:IOTMAP>2.0.CO;2.

Baturin, N. G., and P. P. Niiler, 1997: Effects of instability waves in the mixed layer of the equatorial Pacific. *J. Geophys. Res.*, **102**, 27 771–27 793, https://doi.org/10.1029/97JC02455.

Becker, J. J., and Coauthors, 2009: Global bathymetry and elevation data at 30 arc seconds resolution: SRTM30_PLUS. *Mar. Geod.*, **32**, 355–371, https://doi.org/10.1080/01490410903297766.

Bosc, C., and T. Delcroix, 2008: Observed equatorial Rossby waves and ENSO-related warm water volume changes in the equatorial Pacific Ocean. *J. Geophys. Res.*, **113**, C06003, https://doi.org/10.1029/2007JC004613.

Boucharel, J., and F.-F. Jin, 2020: A simple theory for the modulation of tropical instability waves by ENSO and the annual cycle. *Tellus*, **72A**, 1–14, https://doi.org/10.1080/16000870.2019.1700087.

——, A. Timmermann, and F.-F. Jin, 2013: Zonal phase propagation of ENSO sea surface temperature anomalies: Revisited. *Geophys. Res. Lett.*, **40**, 4048–4053, https://doi.org/10.1002/grl.50685.

——, F.-F. Jin, M. H. England, B. Dewitte, I. I. Lin, H.-C. Huang, and M. A. Balmaseda, 2016: Influence of oceanic intraseasonal Kelvin waves on eastern Pacific hurricane activity. *J. Climate*, **29**, 7941–7955, https://doi.org/10.1175/JCLI-D-16-0112.1.

Bryan, K., J. K. Dukowicz, and R. D. Smith, 1999: On the mixing coefficient in the parameterization of bolus velocity. *J. Phys. Oceanogr.*, **29**, 2442–2456, https://doi.org/10.1175/1520-0485(1999)029<2442:OTMCIT>2.0.CO;2.

Bryden, H. L., and E. C. Brady, 1989: Eddy momentum and heat fluxes and their effects on the circulation of the equatorial Pacific Ocean. *J. Mar. Res.*, **47**, 55–79, https://doi.org/10.1357/002224089785076389.

Cane, M., and E. Sarachik, 1977: Forced baroclinic ocean motions. II-the linear equatorial bounded case. *J. Mar. Res.*, **35**, 395–432,

Carton, J. A., G. A. Chepurin, L. Chen, S. Grodsky, E. Kalnay, and S. G. Penny, 2019: Soda project: SODA3 ensemble

means and standard deviations. Research Data Archive at the National Center for Atmospheric Research, Computational and Information Systems Laboratory, accessed March 2021, https://doi.org/10.5065/HBTB-R521.

Chavez, F. P., P. G. Strutton, G. E. Friederich, R. A. Feely, G. C. Feldman, D. G. Foley, and M. J. McPhaden, 1999: Biological and chemical response of the equatorial Pacific Ocean to the 1997–98 El Niño. *Science*, **286**, 2126–2131, https://doi.org/10.1126/science.286.5447.2126.

Chelton, D. B., and Coauthors, 2001: Observations of coupling between surface wind stress and sea surface temperature in the eastern tropical Pacific. *J. Climate*, **14**, 1479–1498, https://doi.org/10.1175/1520-0442(2001)014<1479:OOCBSW>2.0.CO;2.

Cherian, D. A., D. B. Whitt, R. M. Holmes, R.-C. Lien, S. D. Bachman, and W. G. Large, 2021: Off-equatorial deep-cycle turbulence forced by tropical instability waves in the equatorial Pacific. *J. Phys. Oceanogr.*, **51**, 1575–1593, https://doi.org/10.1175/JPO-D-20-0229.1.

Contreras, R. F., 2002: Long-term observations of tropical instability waves. *J. Phys. Oceanogr.*, **32**, 2715–2722, https://doi.org/10.1175/1520-0485(2002)032<2715:LTOOTI>2.0.CO;2.

Cox, M., 1980: Generation and propagation of 30-day waves in a numerical model of the Pacific. *J. Phys. Oceanogr.*, **10**, 1168–1186, https://doi.org/10.1175/1520-0485(1980)010<1168:GAPODW>2.0.CO;2.

Debreu, L., P. Marchesiello, P. Penven, and G. Cambon, 2012: Two-way nesting in split-explicit ocean models: Algorithms, implementation and validation. *Ocean Modell.*, **49–50**, 1–21, https://doi.org/10.1016/j.ocemod.2012.03.003.

Delpech, A., S. Cravatte, F. Marin, C. Ménesguen, and Y. Morel, 2020: Deep eddy kinetic energy in the tropical Pacific from Lagrangian floats. *J. Geophys. Res. Oceans*, **125**, e2020JC016313, https://doi.org/10.1029/2020JC016313.

Dolinar, E. K., X. Dong, and B. Xi, 2016: Evaluation and intercomparison of clouds, precipitation, and radiation budgets in recent reanalyses using satellite-surface observations. *Climate Dyn.*, **46**, 2123–2144, https://doi.org/10.1007/s00382-015-2693-z.

Düing, W., and Coauthors, 1975: Meanders and long waves in the equatorial Atlantic. *Nature*, **257**, 280–284, https://doi.org/10.1038/257280a0.

Escobar-Franco, M. G., J. Boucharel, and B. Dewitte, 2022: On the relationship between tropical instability waves and intraseasonal equatorial Kelvin waves in the Pacific from satellite observations (1993–2018). *Front. Mar. Sci.*, **9**, 788908, https://doi.org/10.3389/fmars.2022.788908.

Evans, W., P. G. Strutton, and F. P. Chavez, 2009: Impact of tropical instability waves on nutrient and chlorophyll distributions in the equatorial Pacific. *Deep-Sea Res. I*, **56**, 178–188, https://doi.org/10.1016/j.dsr.2008.08.008.

Fairall, C. W., E. F. Bradley, J. E. Hare, A. A. Grachev, and J. B. Edson, 2003: Bulk parameterization of air–sea fluxes: Updates and verification for the COARE algorithm. *J. Climate*, **16**, 571–591, https://doi.org/10.1175/1520-0442(2003)016<0571:BPOASF>2.0.CO;2.

Flament, P. J., S. C. Kennan, R. A. Knox, P. P. Niiler, and R. L. Bernstein, 1996: The three-dimensional structure of an upper ocean vortex in the tropical Pacific Ocean. *Nature*, **383**, 610–613, https://doi.org/10.1038/383610a0.

Gent, P. R., and J. C. Mcwilliams, 1990: Isopycnal mixing in ocean circulation models. *J. Phys. Oceanogr.*, **20**, 150–155, https://doi.org/10.1175/1520-0485(1990)020<0150:IMIOCM>2.0.CO;2.

——, J. Willebrand, T. J. McDougall, and J. C. McWilliams, 1995: Parameterizing eddy-induced tracer transports in ocean circulation models. *J. Phys. Oceanogr.*, **25**, 463–474, https://doi.org/10.1175/1520-0485(1995)025<0463:PEITTI>2.0.CO;2.

Giese, B. S., and D. E. Harrison, 1991: Eastern equatorial Pacific response to three composite westerly wind types. *J. Geophys. Res.*, **96**, 3239–3248, https://doi.org/10.1029/90JC01861.

Graham, T., 2014: The importance of eddy permitting model resolution for simulation of the heat budget of tropical instability waves. *Ocean Modell.*, **79**, 21–32, https://doi.org/10.1016/j.ocemod.2014.04.005.

Gushchina, D., and B. Dewitte, 2012: Intraseasonal tropical atmospheric variability associated with the two flavors of El Niño. *Mon. Wea. Rev.*, **140**, 3669–3681, https://doi.org/10.1175/MWR-D-11-00267.1.

Halpern, D., R. A. Knox, and D. S. Luther, 1988: Observations of 20-day period meridional current oscillations in the upper ocean along the Pacific equator. *J. Phys. Oceanogr.*, **18**, 1514–1534, https://doi.org/10.1175/1520-0485(1988)018<1514:OODPMC>2.0.CO;2.

Harrison, D. E., and B. S. Giese, 1988: Remote westerly wind forcing of the eastern equatorial Pacific; Some model results. *Geophys. Res. Lett.*, **15**, 804–807, https://doi.org/10.1029/GL015i008p00804.

Hashizume, H., S.-P. Xie, W. T. Liu, and K. Takeuchi, 2001: Local and remote atmospheric response to tropical instability waves: A global view from space. *J. Geophys. Res.*, **106**, 10 173–10 185, https://doi.org/10.1029/2000JD900684.

Holmes, R. M., and L. N. Thomas, 2015: The modulation of equatorial turbulence by tropical instability waves in a regional ocean model. *J. Phys. Oceanogr.*, **45**, 1155–1173, https://doi.org/10.1175/JPO-D-14-0209.1.

——, and ——, 2016: Modulation of tropical instability wave intensity by equatorial Kelvin waves. *J. Phys. Oceanogr.*, **46**, 2623–2643, https://doi.org/10.1175/JPO-D-16-0064.1.

Im, S.-H., S.-I. An, M. Lengaigne, and Y. Noh, 2012: Seasonality of tropical instability waves and its feedback to the seasonal cycle in the tropical eastern Pacific. *Sci. World J.*, **2012**, 612048, https://doi.org/10.1100/2012/612048.

Imada, Y., and M. Kimoto, 2012: Parameterization of tropical instability waves and examination of their impact on ENSO characteristics. *J. Climate*, **25**, 4568–4581, https://doi.org/10.1175/JCLI-D-11-00233.1.

Inoue, R., R.-C. Lien, and J. N. Moum, 2012: Modulation of equatorial turbulence by a tropical instability wave. *J. Geophys. Res.*, **117**, C10009, https://doi.org/10.1029/2011JC007767.

——, ——, ——, R. C. Perez, and M. C. Gregg, 2019: Variations of equatorial shear, stratification, and turbulence within a tropical instability wave cycle. *J. Geophys. Res. Oceans*, **124**, 1858–1875, https://doi.org/10.1029/2018JC014480.

Jin, F.-F., 1997a: An equatorial ocean recharge paradigm for ENSO. Part I: Conceptual model. *J. Atmos. Sci.*, **54**, 811–829, https://doi.org/10.1175/1520-0469(1997)054<0811:AEORPF>2.0.CO;2.

——, 1997b: An equatorial ocean recharge paradigm for ENSO. Part II: A stripped-down coupled model. *J. Atmos. Sci.*, **54**, 830–847, https://doi.org/10.1175/1520-0469(1997)054<0830:AEORPF>2.0.CO;2.

——, 2003: Strong El Niño events and nonlinear dynamical heating. *Geophys. Res. Lett.*, **30**, 1120, https://doi.org/10.1029/2002GL016356.

Jing, Z., L. Wu, D. Wu, and B. Qiu, 2014: Enhanced 2-h–8-day oscillations associated with tropical instability waves. *J. Phys. Oceanogr.*, **44**, 1908–1918, https://doi.org/10.1175/JPO-D-13-0189.1.

Jochum, M., and R. Murtugudde, 2006: Temperature advection by tropical instability waves. *J. Phys. Oceanogr.*, **36**, 592–605, https://doi.org/10.1175/JPO2870.1.

——, M. F. Cronin, W. S. Kessler, and D. Shea, 2007: Observed horizontal temperature advection by tropical instability waves. *Geophys. Res. Lett.*, **34**, L09604, https://doi.org/10.1029/2007GL029416.

Johnson, G. C., B. M. Sloyan, W. S. Kessler, and K. E. McTaggart, 2002: Direct measurements of upper ocean currents and water properties across the tropical Pacific during the 1990s. *Prog. Oceanogr.*, **52**, 31–61, https://doi.org/10.1016/S0079-6611(02)00021-6.

Kennan, S. C., and P. J. Flament, 2000: Observations of a tropical instability vortex. *J. Phys. Oceanogr.*, **30**, 2277–2301, https://doi.org/10.1175/1520-0485(2000)030<2277:OOATIV>2.0.CO;2.

Kessler, W. S., 2006: The circulation of the eastern tropical Pacific: A review. *Prog. Oceanogr.*, **69**, 181–217, https://doi.org/10.1016/j.pocean.2006.03.009.

——, L. M. Rothstein, and D. Chen, 1998: The annual cycle of SST in the eastern tropical Pacific, diagnosed in an ocean GCM. *J. Climate*, **11**, 777–799, https://doi.org/10.1175/1520-0442(1998)011<0777:TACOSI>2.0.CO;2.

Large, W. G., J. C. McWilliams, and S. C. Doney, 1994: Oceanic vertical mixing: A review and a model with a nonlocal boundary layer parameterization. *Rev. Geophys.*, **32**, 363, https://doi.org/10.1029/94RG01872.

Laurindo, L. C., A. J. Mariano, and R. Lumpkin, 2017: An improved near-surface velocity climatology for the global ocean from drifter observations. *Deep-Sea Res. I*, **124**, 73–92, https://doi.org/10.1016/j.dsr.2017.04.009.

Legeckis, R., 1977: Long waves in the eastern equatorial Pacific Ocean: A view from a geostationary satellite. *Science*, **197**, 1179–1181, https://doi.org/10.1126/science.197.4309.1179.

——, C. W. Brown, F. Bonjean, and E. S. Johnson, 2004: The influence of tropical instability waves on phytoplankton blooms in the wake of the Marquesas Islands during 1998 and on the currents observed during the drift of the Kon-Tiki in 1947. *Geophys. Res. Lett.*, **31**, L23307, https://doi.org/10.1029/2004GL021637.

Lien, R.-C., E. A. D'Asaro, and C. E. Menkes, 2008: Modulation of equatorial turbulence by tropical instability waves. *Geophys. Res. Lett.*, **35**, L24607, https://doi.org/10.1029/2008GL035860.

Lyman, J. M., G. C. Johnson, and W. S. Kessler, 2007: Distinct 17- and 33-day tropical instability waves in subsurface observations. *J. Phys. Oceanogr.*, **37**, 855–872, https://doi.org/10.1175/JPO3023.1.

Madden, R. A., and P. R. Julian, 1994: Observations of the 40–50-day tropical oscillation—A review. *Mon. Wea. Rev.*, **122**, 814–837, https://doi.org/10.1175/1520-0493(1994)122<0814:OOTDTO>2.0.CO;2.

Malardé, J.-P., C. Perigaud, P. D. Mey, and J.-F. Minster, 1987: Observation of long equatorial waves in the Pacific Ocean by SEASAT altimetry. *J. Phys. Oceanogr.*, **17**, 2273–2279, https://doi.org/10.1175/1520-0485(1987)017<2273:OOLEWI>2.0.CO;2.

Maloney, E. D., and J. T. Kiehl, 2002: MJO-related SST variations over the tropical eastern Pacific during Northern Hemisphere summer. *J. Climate*, **15**, 675–689, https://doi.org/10.1175/1520-0442(2002)015<0675:MRSVOT>2.0.CO;2.

Marchesiello, P., X. Capet, C. Menkes, and S. C. Kennan, 2011: Submesoscale dynamics in tropical instability waves. *Ocean Modell.*, **39**, 31–46, https://doi.org/10.1016/j.ocemod.2011.04.011.

Masina, S., and S. G. H. Philander, 1999: An analysis of tropical instability waves in a numerical model of the Pacific Ocean: 1. Spatial variability of the waves. *J. Geophys. Res.*, **104**, 29 613–29 635, https://doi.org/10.1029/1999JC900227.

——, ——, and A. B. G. Bush, 1999: An analysis of tropical instability waves in a numerical model of the Pacific Ocean: 2. Generation and energetics of the waves. *J. Geophys. Res.*, **104**, 29 637–29 661, https://doi.org/10.1029/1999JC900226.

McPhaden, M. J., 1996: Monthly period oscillations in the Pacific north equatorial countercurrent. *J. Geophys. Res.*, **101**, 6337–6359, https://doi.org/10.1029/95JC03620.

——, and X. Yu, 1999: Equatorial waves and the 1997–98 El Niño. *Geophys. Res. Lett.*, **26**, 2961–2964, https://doi.org/10.1029/1999GL004901.

Menkes, C. E. R., J. G. Vialard, S. C. Kennan, J.-P. Boulanger, and G. V. Madec, 2006: A modeling study of the impact of tropical instability waves on the heat budget of the eastern equatorial Pacific. *J. Phys. Oceanogr.*, **36**, 847–865, https://doi.org/10.1175/JPO2904.1.

Miller, L., D. R. Watts, and M. Wimbush, 1985: Oscillations of dynamic topography in the eastern equatorial Pacific. *J. Phys. Oceanogr.*, **15**, 1759–1770, https://doi.org/10.1175/1520-0485(1985)015<1759:OODTIT>2.0.CO;2.

Moum, J. N., R.-C. Lien, A. Perlin, J. D. Nash, M. C. Gregg, and P. J. Wiles, 2009: Sea surface cooling at the equator by subsurface mixing in tropical instability waves. *Nat. Geosci.*, **2**, 761–765, https://doi.org/10.1038/ngeo657.

Musman, S., 1989: Sea height wave form in equatorial waves and its interpretation. *J. Geophys. Res.*, **94**, 3303–3309, https://doi.org/10.1029/JC094iC03p03303.

Périgaud, C., 1990: Sea level oscillations observed with Geosat along the two shear fronts of the Pacific north equatorial countercurrent. *J. Geophys. Res.*, **95**, 7239–7248, https://doi.org/10.1029/JC095iC05p07239.

Philander, S. G. H., 1976: Instabilities of zonal equatorial currents. *J. Geophys. Res.*, **81**, 3725–3735, https://doi.org/10.1029/JC081i021p03725.

——, 1978: Instabilities of zonal equatorial currents, 2. *J. Geophys. Res.*, **83**, 3679–3682, https://doi.org/10.1029/JC083iC07p03679.

——, 1990: *El Niño, La Niña, and the Southern Oscillation*. Academic Press, 293 pp.

Praveen Kumar, B., J. Vialard, M. Lengaigne, V. S. N. Murty, and M. J. McPhaden, 2012: TropFlux: Air-sea fluxes for the global tropical oceans—Description and evaluation. *Climate Dyn.*, **38**, 1521–1543, https://doi.org/10.1007/s00382-011-1115-0.

Qiao, L., and R. H. Weisberg, 1995: Tropical instability wave kinematics: Observations from the tropical instability wave experiment. *J. Geophys. Res.*, **100**, 8677–8693, https://doi.org/10.1029/95JC00305.

——, and ——, 1998: Tropical instability wave energetics: Observations from the tropical instability wave experiment. *J. Phys. Oceanogr.*, **28**, 345–360, https://doi.org/10.1175/1520-0485(1998)028<0345:TIWEOF>2.0.CO;2.

Renault, L., M. J. Molemaker, J. C. Mcwilliams, A. F. Shchepetkin, F. Lemari, D. Chelton, S. Illig, and A. Hall, 2016: Modulation of wind work by oceanic current interaction with the atmosphere. *J. Phys. Oceanogr.*, **46**, 1685–1704, https://doi.org/10.1175/JPO-D-15-0232.1.

——, P. Marchesiello, S. Masson, and J. C. McWilliams, 2019: Remarkable control of western boundary currents by *eddy killing,* a mechanical air-sea coupling process. *Geophys. Res. Lett.*, **46**, 2743–2751, https://doi.org/10.1029/2018GL081211.

——, S. Masson, T. Arsouze, G. Madec, and J. C. McWilliams, 2020: Recipes for how to force oceanic model dynamics. *J. Adv. Model. Earth Syst.*, **12**, e2019MS001715, https://doi.org/10.1029/2019MS001715.

Rio, M.-H., S. Mulet, and N. Picot, 2014: Beyond GOCE for the ocean circulation estimate: Synergetic use of altimetry, gravimetry, and in situ data provides new insight into geostrophic and Ekman currents. *Geophys. Res. Lett.*, **41**, 8918–8925, https://doi.org/10.1002/2014GL061773.

Roberts, M. J., and Coauthors, 2004: Impact of an eddy-permitting ocean resolution on control and climate change simulations with a global coupled GCM. *J. Climate*, **17**, 3–20, https://doi.org/10.1175/1520-0442(2004)017<0003:IOAEOR>2.0.CO;2.

——, and Coauthors, 2009: Impact of resolution on the tropical Pacific circulation in a matrix of coupled models. *J. Climate*, **22**, 2541–2556, https://doi.org/10.1175/2008JCLI2537.1.

Saha, S., and Coauthors, 2010: NCEP Climate Forecast System Reanalysis (CFSR) selected hourly time-series products, January 1979 to December 2010. Research Data Archive at the National Center for Atmospheric Research, Computational and Information Systems Laboratory, accessed February 2021, https://doi.org/10.5065/D6513W89.

——, and Coauthors, 2011: NCEP Climate Forecast System version 2 (CFSV2) selected hourly time-series products. Research Data Archive at the National Center for Atmospheric Research, Computational and Information Systems Laboratory, accessed February 2021, https://doi.org/10.5065/D6N877VB.

Seo, H., M. Jochum, R. Murtugudde, A. J. Miller, and J. O. Roads, 2007: Feedback of tropical instability-wave-induced atmospheric variability onto the ocean. *J. Climate*, **20**, 5842–5855, https://doi.org/10.1175/JCLI4330.1.

Shchepetkin, A. F., 2015: An adaptive, Courant-number-dependent implicit scheme for vertical advection in oceanic modeling. *Ocean Modell.*, **91**, 38–69, https://doi.org/10.1016/j.ocemod.2015.03.006.

——, and J. C. McWilliams, 2005: The Regional Oceanic Modeling System (ROMS): A split-explicit, free-surface, topography-following-coordinate oceanic model. *Ocean Modell.*, **9**, 347–404, https://doi.org/10.1016/j.ocemod.2004.08.002.

——, and ——, 2009: Correction and commentary for "Ocean fore-casting in terrain-following coordinates: Formulation and skill assessment of the regional ocean modeling system" by Haidvogel et al., J. Comp. Phys. 227, pp. 3595–3624. *J. Comput. Phys.*, **228**, 8985–9000, https://doi.org/10.1016/j.jcp.2009.09.002.

Small, R. J., K. J. Richards, S.-P. Xie, P. Dutrieux, and T. Miyama, 2009: Damping of tropical instability waves caused by the action of surface currents on stress. *J. Geophys. Res.*, **114**, C04009, https://doi.org/10.1029/2008JC005147.

Strutton, P. G., J. P. Ryan, and F. P. Chavez, 2001: Enhanced chlorophyll associated with tropical instability waves in the equatorial Pacific. *Geophys. Res. Lett.*, **28**, 2005–2008, https://doi.org/10.1029/2000GL012166.

Swenson, M. S., and D. V. Hansen, 1999: Tropical Pacific Ocean mixed layer heat budget: The Pacific cold tongue. *J. Phys. Oceanogr.*, **29**, 69–81, https://doi.org/10.1175/1520-0485(1999)029<0069:TPOMLH>2.0.CO;2.

Tanaka, Y., and T. Hibiya, 2019: Generation mechanism of tropical instability waves in the equatorial Pacific Ocean. *J. Phys. Oceanogr.*, **49**, 2901–2915, https://doi.org/10.1175/JPO-D-19-0094.1.

Taylor, K. E., 2001: Summarizing multiple aspects of model performance in a single diagram. *J. Geophys. Res.*, **106**, 7183–7192, https://doi.org/10.1029/2000JD900719.

Valdivieso, M., and Coauthors, 2017: An assessment of air–sea heat fluxes from ocean and coupled reanalyses. *Climate Dyn.*, **49**, 983–1008, https://doi.org/10.1007/s00382-015-2843-3.

Vialard, J. R. M., C. Menkes, J.-P. Boulanger, P. Delecluse, E. Guilyardi, M. J. Mcphaden, and G. Madec, 2001: A model study of oceanic mechanisms affecting equatorial Pacific sea surface temperature during the 1997–98 El Niño. *J. Phys. Oceanogr.*, **31**, 1649–1675, https://doi.org/10.1175/1520-0485(2001)031<1649:AMSOOM>2.0.CO;2.

von Schuckmann, K., P. Brandt, and C. Eden, 2008: Generation of tropical instability waves in the Atlantic Ocean. *J. Geophys. Res.*, **113**, C08034, https://doi.org/10.1029/2007JC004712.

Wang, C., and P. C. Fiedler, 2006: ENSO variability and the eastern tropical Pacific: A review. *Prog. Oceanogr.*, **69**, 239–266, https://doi.org/10.1016/j.pocean.2006.03.004.

Wang, M., Y. Du, B. Qiu, X. Cheng, Y. Luo, X. Chen, and M. Feng, 2017: Mechanism of seasonal eddy kinetic energy variability in the eastern equatorial Pacific Ocean. *J. Geophys. Res. Oceans*, **122**, 3240–3252, https://doi.org/10.1002/2017JC012711.

——, ——, ——, S.-P. Xie, and M. Feng, 2019: Dynamics on seasonal variability of EKE associated with TIWs in the eastern equatorial Pacific Ocean. *J. Phys. Oceanogr.*, **49**, 1503–1519, https://doi.org/10.1175/JPO-D-18-0163.1.

——, S.-P. Xie, S. S. P. Shen, and Y. Du, 2020: Rossby and Yanai modes of tropical instability waves in the equatorial Pacific Ocean and a diagnostic model for surface currents. *J. Phys. Oceanogr.*, **50**, 3009–3024, https://doi.org/10.1175/JPO-D-20-0063.1.

Wang, W., P. Xie, S.-H. Yoo, Y. Xue, A. Kumar, and X. Wu, 2011: An assessment of the surface climate in the NCEP Climate Forecast System Reanalysis. *Climate Dyn.*, **37**, 1601–1620, https://doi.org/10.1007/s00382-010-0935-7.

Warner, S. J., R. M. Holmes, E. H. M. Hawkins, M. S. Hoecker-Martínez, A. C. Savage, and J. N. Moum, 2018: Buoyant gravity currents released from tropical instability waves. *J. Phys. Oceanogr.*, **48**, 361–382, https://doi.org/10.1175/JPO-D-17-0144.1.

Wei, Y., Y. Pei, and X. Kang, 2019: Assessing feedback of tropical instability wave-induced wind stress perturbations in the equatorial Pacific. *Int. J. Climatol.*, **39**, 1634–1643, https://doi.org/10.1002/joc.5906.

Xie, S.-P., M. Ishiwatari, H. Hashizume, and K. Takeuchi, 1998: Coupled ocean-atmospheric waves on the equatorial front. *Geophys. Res. Lett.*, **25**, 3863–3866, https://doi.org/10.1029/1998GL900014.

Xue, A., F.-F. Jin, W. Zhang, J. Boucharel, S. Zhao, and X. Yuan, 2020: Delineating the seasonally modulated nonlinear feedback onto ENSO from tropical instability waves. *Geophys. Res. Lett.*, **47**, e2019GL085863, https://doi.org/10.1029/2019GL085863.

——, W. Zhang, J. Boucharel, and F.-F. Jin, 2021: Anomalous tropical instability wave activity hindered the development of the 2016/17 La Niña. *J. Climate*, **34**, 5583–5600, https://doi.org/10.1175/JCLI-D-20-0399.1.

Yeager, S. G., and W. G. Large, 2008: CORE.2 global air-sea flux dataset. Research Data Archive at the National Center for Atmospheric Research, Computational and Information Systems Laboratory, accessed May 2021, https://doi.org/10.5065/D6WH2N0S.

Yoder, J. A., S. G. Ackleson, R. T. Barber, P. Flament, and W. M. Balch, 1994: A line in the sea. *Nature*, **371**, 689–692, https://doi.org/10.1038/371689a0.

Yu, J.-Y., and W. T. Liu, 2003: A linear relationship between ENSO intensity and tropical instability wave activity in the eastern Pacific Ocean. *Geophys. Res. Lett.*, **30**, 1735, https://doi.org/10.1029/2003GL017176.

Yu, Z., J. P. McCreary, and J. A. Proehl, 1995: Meridional asymmetry and energetics of tropical instability waves. *J. Phys. Oceanogr.*, **25**, 2997–3007, https://doi.org/10.1175/1520-0485(1995)025<2997:MAAEOT>2.0.CO;2.